UCRL-53728
Distribution Category UC-70

UCRL--53728

DE87 013822

Post-Test Thermal Calculations and Data Analyses for the Spent Fuel Test—Climax

D. N. Montan

W. C. Patrick

Manuscript date: June 1986

LAWRENCE LIVERMORE NATIONAL LABORATORY
University of California • Livermore, California • 94550

Available from: National Technical Information Service • U.S. Department of Commerce
5285 Port Royal Road • Springfield, VA 22161 • A03 • (Microfiche A01)

Contents

POST-TEST THERMAL CALCULATIONS AND DATA ANALYSES FOR THE SPENT FUEL TEST--CLIMAX

ABSTRACT

The Spent Fuel Test--Climax (SFT-C) provided an opportunity to evaluate the feasibility of retrievable, deep geologic storage of spent-fuel assemblies from commercial nuclear reactors. Several heat-transfer models and analytical solutions were used to design the test and to evaluate its performance. In the process, the models were also evaluated. While we found excellent agreement between measured and calculated temperatures, some aspects of the heat-transfer calculations needed refinement.

After the SFT-C was completed, additional calculations were performed using the best available (directly measured or inferred from measurements made during the test) input parameters, thermal properties, and power levels. This report documents those calculations and compares the results with measurements made during the three-year heating phase and six-month posttest cooling phase of the SFT-C. Results from three basic types of heat-transfer calculations are presented:

- A combined two-dimensional/three-dimensional, infinite-length, finite-difference model;
- A fully three-dimensional, finite-length, finite-difference model;
- A fully three-dimensional, finite-length, analytical solution.

Results indicate that the finite-length model much more accurately reflects heat flow near the ends of the array and produces cooler temperatures everywhere than does its infinite-length counterpart. Capturing the near-field phenomena, even with a detailed three-dimensional model of the emplacement geometry, has been impossible. Even so, we believe that the errors observed (a few degrees celsius) indicate that the modeling is adequate for use in future tests and for designing repositories.

Successful calculation of the ventilation process has also been elusive. However, we found that the results were quite insensitive to fairly wide variations in both basic thermal properties and ventilation flow rate. This suggests that reasonable estimates of these properties from laboratory testing--or, in some cases, handbook values--will be adequate for most design purposes.

1 INTRODUCTION

A test of retrievable dry geologic storage of spent-fuel assemblies from an operating commercial nuclear reactor was recently completed in a granitic intrusive at the U.S. Department of Energy's (DOE) Nevada Test Site. Generally referred to as the Spent Fuel Test--Climax (SFT-C), this project is part of the Nevada Nuclear Waste Storage Investigations, which are managed by the Nevada Operations Office of the DOE. The Lawrence Livermore National Laboratory (LLNL) was responsible for the technical direction of the test (Ramspott et al., 1979) and is in the process of documenting the results of the SFT-C (Patrick, 1986).

In addition to evaluating the feasibility of deep geologic storage, the test provided an excellent opportunity to study heat-transfer processes on a large scale. Specific objectives related to heat transfer were to:

- Simulate the effect of thousands of canisters of spent-nuclear-fuel assemblies by using only a few assemblies augmented with electrical heaters.
- Evaluate any differences in the effects on the test environment of a radioactive waste source and an electrically heated simulator.
- Document the thermal energy removed in the ventilation airstream.
- Document the response of the rock mass to extensive heating.

To attain these objectives, it was necessary to accurately calculate heat transfer from various thermal sources through the rock mass and into the ventilation airstream. Previously reported calculations (Montan and Patrick, 1981) provided a basis for test design and for siting instrumentation throughout the test array. Although several codes were used in the design process, our workhorse was the finite-difference code (sometimes referred to as an integrated finite-difference code) TRUMP and its associated preprocessor and postprocessor (Edwards, 1972). For these calculations, the near-field environment around the individual spent-fuel canisters was modeled in three dimensions with conduction, convection, and thermal radiation treated explicitly. Outside this region, heat flow was modeled in two dimensions. The removal of energy by the ventilation airstream was treated with a novel partial-flow model in which the unit cell of the calculation receives a fraction of the total flow rate. In this model, air enters the cell at ambient temperature and leaves at the average air temperature of the cell. Montan and Patrick (1981) reported on the design calculations and included details of these models.

As the SFT-C progressed and data were obtained and analyzed, it became clear that the design calculations simulated the conditions present in the test array quite well (Patrick et al., 1982, 1983, and 1984a). Calculated and measured temperatures agreed within a few degrees throughout the 10,000-m^3 instrumented volume of rock. An exception was the calculation of energy removed by the ventilation airstream. While the calculation indicated that the rate of energy removal increased monotonically with time, the measurements indicated that the removal rate was nearly constant.

This report has two purposes:

- First, it documents our attempts to improve upon the design calculations by incorporating such refinements as energy deposition and ventilation flow rates measured during the test, cooling of the rock mass as a result of pretest construction, and measured ambient rock temperatures. In addition, we examine the influence of variations in several heat-transfer properties on the distribution of temperatures throughout the test array. Most calculations were done with the TRUMP model described above. We also simulated the SFT-C with two finite-length models: one based on analytical solutions and the other a finite-difference approach. These models allow examination of heat flow near the ends of the SFT-C array, where the assumptions of infinite length are clearly violated.
- Second, it presents and analyzes the temperature and energy removal measurements in the context of these calculations.

2 TEST DESCRIPTION AND GEOMETRY

2.1 LOCATION AND CONFIGURATION

The SFT-C is located 420 m below ground in the quartz monzonite unit of the Climax stock. At the test level, the rock is moderately to heavily fractured and partially saturated (Wilder and Yow, 1984). Previous testing in the Climax stock determined that the conductivity and diffusivity of the rock, on the scale of several meters, were 3.1 W/m•K and 1.2 mm^2/s, respectively (Montan and Bradkin, 1984). These measurements formed the basis for design calculations and the starting point for studying the sensitivity of the calculations to variations in these properties.

The basic configuration of the test is shown in Fig. 1. Eleven canisters containing single, intact, spent-fuel assemblies, aged about 2.5

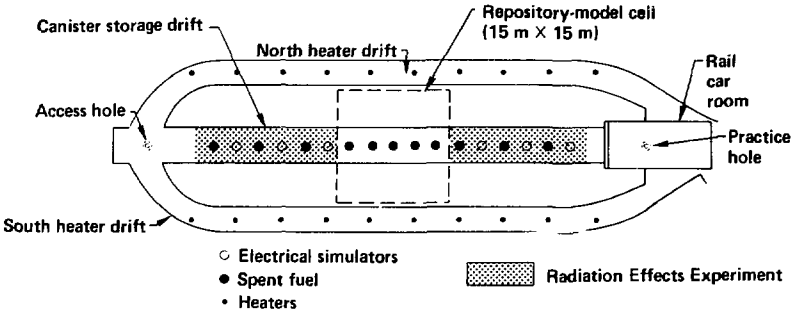

Figure 1. Plan view of the Spent Fuel Test--Climax.

years out of core (YOC), were emplaced in boreholes drilled into the floor of the center drift. At either end of this array, spent-fuel assemblies were interspersed with six electrically heated simulators. To simulate the thermal field of a large repository, 10 auxiliary electrical heaters were placed in the floor of each of the 2 drifts that parallel the center drift.

2.2 INSTRUMENTATION

The history of energy deposition during the SFT-C was determined by several means. First, the power history of the spent-fuel assemblies was determined from calculations and the results of calorimetry (Schmittroth et al., 1982). Second, we used electronic control systems to match the power histories of the electrical simulators with those of the actual spent-fuel assemblies. Third, the thermal output of the auxiliary heaters was controlled and measured by Watt transducers. Finally, incidental sources of energy such as facility lighting were measured with Watt transducers (Brough and Patrick, 1982).

Thermocouples were located throughout the test array to measure the distribution of temperatures during the test (Brough and Patrick, 1982). Although these instruments were concentrated near the canister (Fig. 2), they were also located to measure temperatures relatively far from the heat sources (Fig. 3).

We also monitored the characteristics of the ventilation airstream. The "dry bulb" temperatures and the dew points of the inlet and outlet

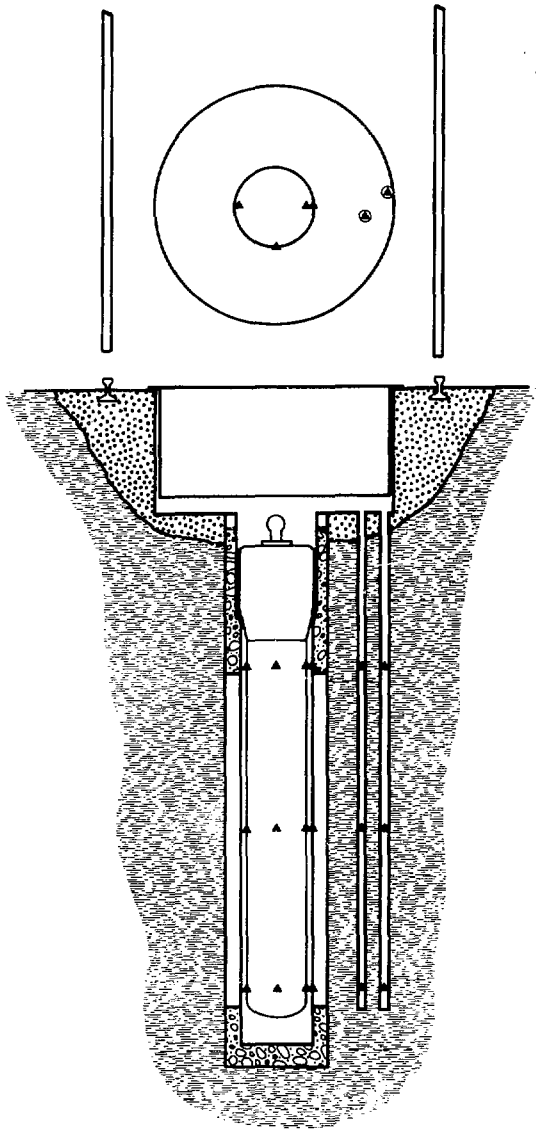

Figure 2. Near-field thermocouple locations are designated with triangles.

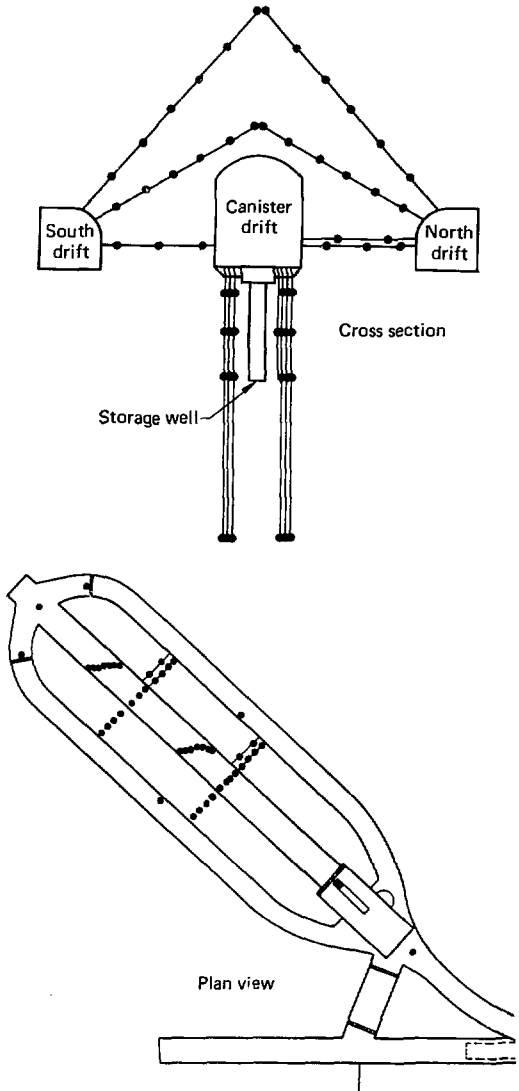

Figure 3. Intermediate-field and far-field thermocouple locations in the storage facility are indicated by dots.

airstreams, together with flow rates, were used to determine the quantity of energy removed by the ventilation system as a function of time.

2.3 ENERGY DEPOSITION AND REMOVAL

When the design calculations for the SFT-C were completed, precise power histories of the spent-fuel, electrical simulators, and auxiliary heaters were unknown. The same is true of variations in the ventilation flow rate and the inlet temperature history of the airstream. However, measurements made during the test were better estimates of the rates of energy deposition and removal for use in the posttest calculations reported here.

The contribution of each source of energy present at the SFT-C is shown in Table 1, and these contributions are shown as a function of time in Fig. 4. Because facility lighting made a relatively minor contribution to the total energy, this source was not treated explicitly in any calculation and is not discussed further.

Our current understanding of the power history of the spent fuel is as indicated in Fig. 5. In this figure, the power table developed by Schmittroth et al. (1982) has been adjusted to bring it into better agreement with calorimetry data obtained early in the test. After the spent

Table 1. Cumulative energy input to the SFT-C by source.

Source	Cumulative energy through retrieval (MW•h)	(% of total)	Cumulative energy through cool-down (MW•h)	(% of total)
PWR fuel assemblies (11)	263.4	25.3	263.4	24.8
Electrical simulators (6)	148.0	14.2	148.0	14.0
Guard heaters (20)	600.6	57.7	600.6	56.7
Facility lights	29.0	2.8	48.0	4.5
Totals	1041.0	100.0	1060.0	100.0

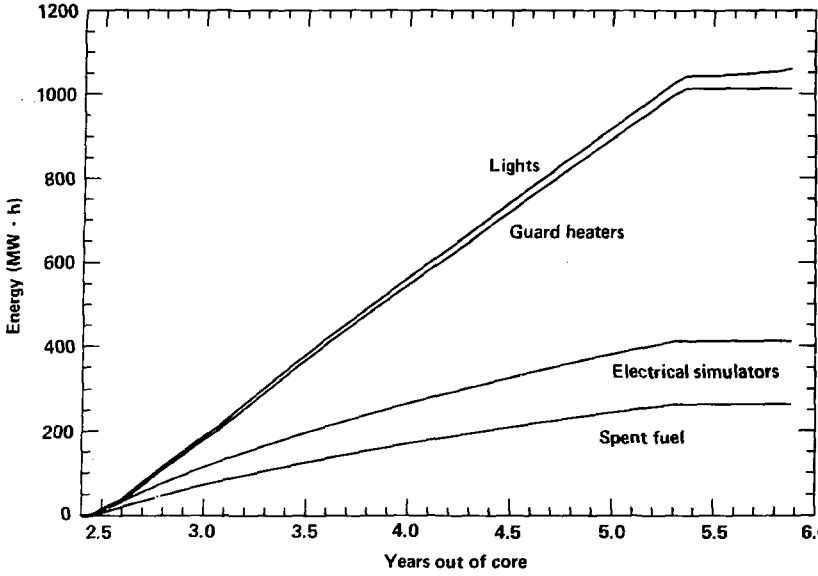

Figure 4. Cumulative thermal energy input by source.

fuel was retrieved, we made two additional calorimetry measurements that agreed with this curve within the accuracy of the measurements.

Also shown in Fig. 5 is the power history of the electrical simulators as measured by Watt transducers. In general, the stair-step of adjustments to the simulator power levels closely matches the decay curve of the spent fuel. Before 3.1 YOC, the simulator power levels were consistently above the decay curve because the original decay curve (at that time unadjusted for calorimetry results) was somewhat higher than the present curve. The resulting error is an insignificant portion of the more than 1 GW•h of energy deposited during the test.

At the beginning of the test, the spent-fuel assemblies were emplaced and the simulators were energized during a six-week period (Table 2). Likewise, at the end of the test they were retrieved or de-energized as appropriate during a similar period of time (Table 3). The assemblies and simulators were treated as individual sources both in the calculations that

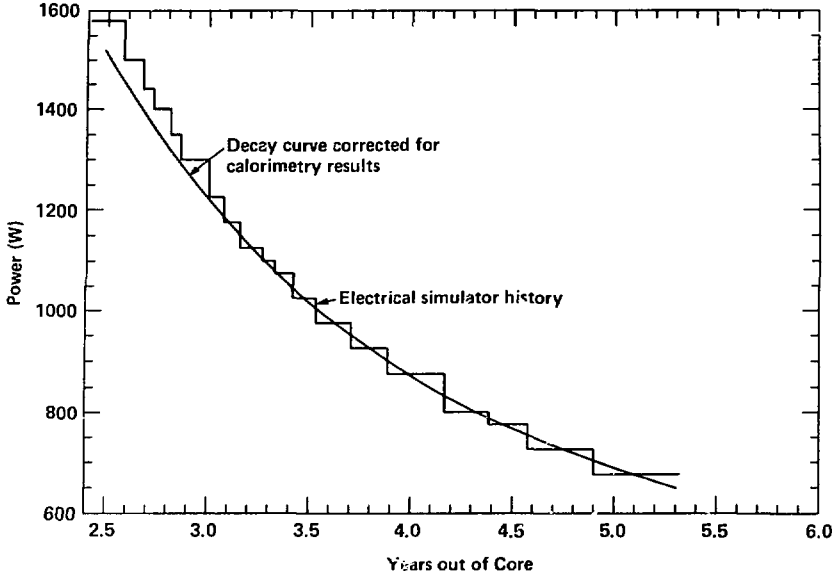

Figure 5. PWR fuel assembly and electrical simulator power history.

Table 2. Schedule for emplacement of spent-fuel and energizing of electrical simulators.

Date 1980	Spent-fuel emplacement		Electrical simulator energized
	Emplacement hole	Serial number	Emplacement hole
18 April	CEH03	D-40	CEH15
22 April	CEH16	D-18	CEH02
25 April	CEH01	D-34	CEH17
19 April	CEH05	D-46	CEH13
1 May	CEH12	D-09	CEH06
6 May	CEH14	D-35	CEH04
8 May	CEH09	D-47	--
13 May	CEH07	D-06	--
15 May	CEH10	D-01	--
20 May	CEH08	D-16	--
28 May	CEH11	D-04	--

Table 3. Schedule for retrieval of spent-fuel and de-energizing of electrical simulators.

Date 1983	Spent-fuel retrieval		Electrical simulator de-energized
	Emplacement hole	Serial number	Emplacement hole
3 March	CEH01	D-34	CEH17
7 March	CEH16	D-22	CEH02
9 March	--	--	CEH15 and CEH13
10 March	CEH03	D-40	--
11 March	--	--	CEH04 and CEH0[illegible]
14 March	CEH05	D-46	--
16 March	CEH14	D-35	--
22 March	CEH12	D-15	--
24 March	CEH09	D-47	--
29 March	CEH07	D-09	--
31 March	CEH11	D-18	--
4 April	CEH08	D-16	--
6 April	CEH10	D-01	--

modeled the facility as an infinite-length array and in the finite-length models, but they were "energized" simultaneously in all the calculations.

The power levels of the auxiliary heaters are shown in Table 4. To simulate the thermal conditions of a panel of a large-scale repository, the power levels of these sources increased as the test progressed. As shown in the data analyses below, the stepwise increases in power closely approximated the thermal pulse that was generated by the interaction of many parallel rows of heat sources in a large repository. Since the

Table 4. Auxiliary heater power history.

Date of change	Power per heater (W)	Comment
27 June 1980	1850	Error
2 July 1980	925	Correct target power level
16 December 1980	1350	Correct target power level
19 February 1982	925	Error
1 March 1982	1400	Power level above target to compensate for error
8 April 1982	1350	Correct target power level
30 March 1983	0	End of heated phase of test

auxiliary heaters were energized and de-energized simultaneously, the timing of their energy deposition was treated explicitly in both finite- and infinite-length representations. Infinite-length models treated the auxiliary heaters in each drift collectively as a strip (or smeared planar) source. The finite-length models treated each auxiliary heater as an individual heat source.

By measuring the characteristics of the inlet and exhaust airstream, we carefully monitored energy removal from the SFT-C. Since one goal was to evaluate our ability to model the removal of thermal energy in the ventilation airstream, we took two different approaches in performing the posttest calculations. First, we used the data on inlet-air temperature in both the finite- and infinite-length representations with the partial-flow ventilation model devised for the TRUMP code (Montan and Patrick, 1981). Calculated and measured energy-removal rates were then compared as discussed below. Second, we used the data on energy removal rate (Fig. 6) as a thermal sink in the finite-length representation with the PLUS family of codes (Montan, 1986). While this latter case does not directly model the ventilation process, it did allow us to compare the quality of agreement between measured and calculated rock temperatures where the energy-removal rates used in the calculation were the same as those measured.

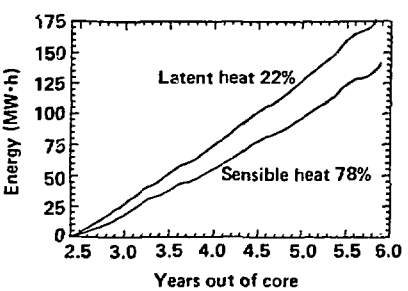

Figure 6. Cumulative thermal energy removed by ventilation.

3 HEAT TRANSFER MODELS OF THE SFT-C

A variety of models, including analytical solutions, were employed during design of the SFT-C (Montan and Patrick, 1981). For the posttest calculations, we used three basic models with a range of values for input parameters. Each model is discussed in turn below.

- A finite-difference model that treated the SFT-C as an infinite-length array and represented the near-field canister environment in three dimensions and the intermediate field in two dimensions.
- A finite-difference model that treated the SFT-C as a finite-length array fully in three dimensions.
- An analytical model that treated the SFT-C as a finite-length array fully in three dimensions.

3.1 INFINITE-ARRAY FINITE-DIFFERENCE MODEL

The workhorse for posttest modeling of the SFT-C--the same basic model used to design the test--is based on a unit cell of an infinitely long array of heat sources. The unit cell, which is defined by two vertical planes perpendicular to the drifts and spaced halfway between the canisters, is further divided by a vertical plane of symmetry that is perpendicular to the drift and passes through the canister center and by a vertical plane of symmetry that is parallel to the axis of the drift and also passes through the canister center. Thus, only one-fourth of the unit cell is modeled.

The mesh used in these calculations contains three basic regions. The innermost Region III (20 m wide by 40 m high) is divided into 1600 zones (each 0.5 by 1 m) to provide the required spatial resolution. Region II (5 by 5 m), consisting of 96 zones, and Region I (20 by 20 m), consisting of 24 zones, were added to give an overall mesh size of 80 by 160 m with a time constant of about 120 years (Fig. 7). The thickness of the zones is 1.5 m or one-half the canister spacing. In the regions comprising the drifts, the regular zoning was replaced by single zones containing air. In addition, 50-mm-thick zones of rock or concrete, as appropriate, were placed on the drift surfaces to obtain accurate surface temperatures for radiation and convection calculations.

Accurate representation of the canister environment required that the relatively large two-dimensional blocks near the heat sources be replaced

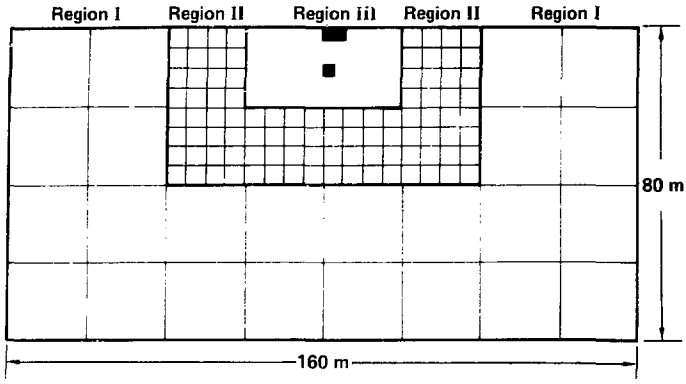

Figure 7. Schematic of mesh used in TRUMP calculations of the infinite-length model.

with a progressively finer three-dimensional mesh. To accomplish this, the 50 two-dimensional zones beneath the floor of the drift to a depth of 10 m were replaced with 150 three-dimensional zones, each measuring 0.5 by 1.0 by 0.5 m. The 54 zones of this set (each 1.5 by 6.0 by 1.5 m) whose midplane coincides with that of the canister were in turn replaced by 486 zones (each 0.17 by 1.0 by 0.17 m). Finally, the 6 corner zones were removed and the surrounding 18 zones were made smaller, leaving the 305-mm-radius borehole in which to place the canister and steel liner. The 230-mm-radius liner was represented by 12 zones varying in height from 0.4 to 0.5 m, and the canister was represented by 11 zones varying in height from 0.2 to 0.5 m. Seven of these zones represent the active heat source of the spent-fuel assembly or electrical simulator.

Heat transport from the canister to the liner and from the liner to the rock was modeled as radiative and convective with emittances of 0.4 (outer canister and inner liner surfaces) and 0.9 (outer liner and rock wall surfaces) (Patrick et al., 1983). Zero-volume zones were placed on the rock surfaces in the borehole to give correct temperatures for the radiative transport calculation. Additional zones were provided to model other details of the test geometry (Montan and Patrick, 1981).

The auxiliary heaters in the side drifts were sufficiently far removed from the main areas of interest that they are modeled in two dimensions. In

this representation, these cylindrical heat sources are "smeared out" so that they are, in effect, strip sources.

3.2 FINITE-ARRAY FINITE-DIFFERENCE MODEL

In an effort to more correctly simulate boundary conditions of the SFT-C, we developed a fully three-dimensional finite-length model of the test array and used the finite-difference code TRUMP to solve the problem. In this model, the single vertical plane of symmetry passes through the center of the spent-fuel storage drift so that only half of the test array is modeled. An adiabatic boundary condition represents this plane of symmetry.

As was the case for the infinite-length array, we constructed a mesh with three regions (Figs. 8 and 9). The innermost Region III (18 m wide by 20 m high by 60 m long) is divided into 19,200 zones (each 0.75 by 1.0 by 1.5 m). This provides the desired spatial resolution in the vicinity of the heat sources and sinks. Region II (3 by 2 by 3 m), consisting of 1968 zones, and Region I (6 by 6 by 6 m), consisting of 1332 zones, were added to provide an overall mesh size of 42 by 72 by 114 with a time constant of

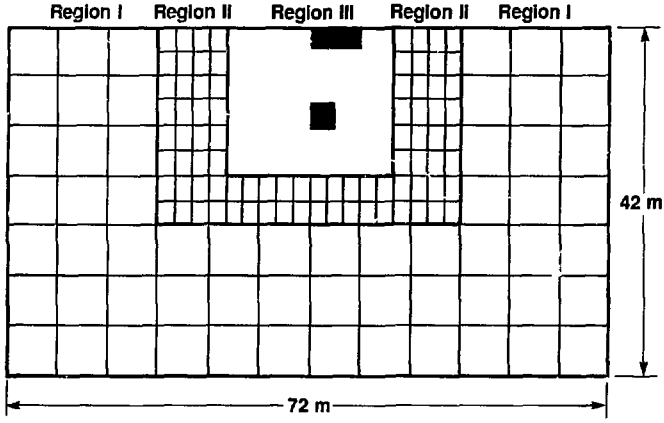

Figure 8. Cross section view of finite-length TRUMP model.

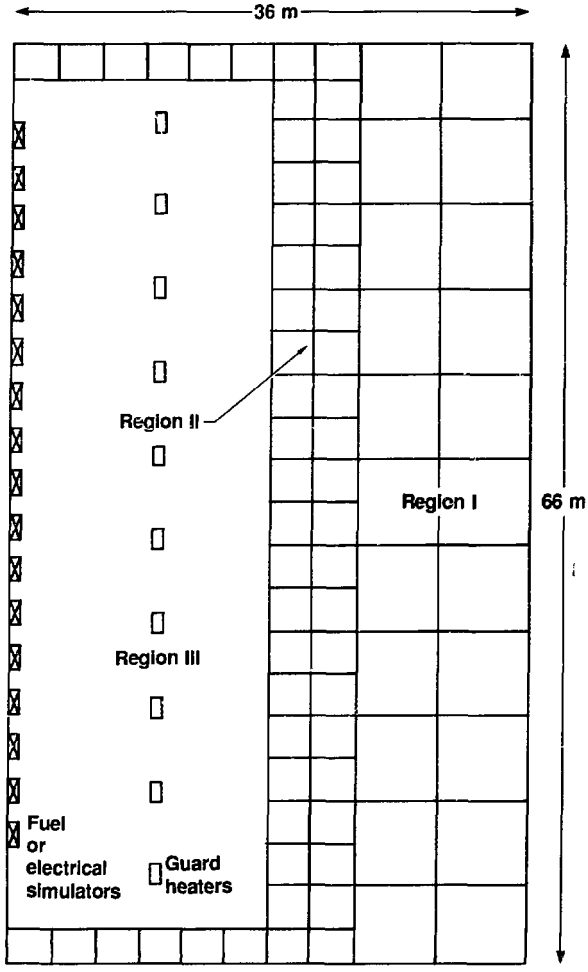

Figure 9. Plan view of finite-length TRUMP model.

about 25 years. The drift openings were treated by assigning effective thermal properties to selected Region III zones.

Because the model size already totaled 22,500 zones, we were unable to incorporate finer zoning in the near-field canister environment. Energy deposition rates to the zones representing spent-fuel canisters and auxiliary heaters were provided in accordance with Fig. 5 and Table 4. Individual emplacement times were not modeled in these calculations.

Radiative heat transfer was treated by assigning the drift zones high thermal conductivities approximating blackbody radiation (Butkovich and Montan, 1980). To approximate the effects of ventilation, we connected selected drift zones to external nodes, the temperatures of which were controlled to approximate the measured air-inlet temperatures.

3.3 FINITE-ARRAY ANALYTICAL MODEL

Another model developed to treat the finite-length aspects of the SFT-C relies on the superposition in time and space of the analytical solution of heat flow from a point source in an infinite medium. We developed and used this model to establish whether the finite-length aspects of the SFT-C (and similar full-scale repository models) could be satisfactorily approximated by this simpler, less computationally intensive formulation.

The basic model considers the rock mass in which the SFT-C is located to be of infinite extent with uniform thermal conductivity 3.11 W/m•K, diffusivity 39.76 m^2/y, and initial temperature 24.7C. The spent-fuel assemblies, electrical simulators, and the 20 auxiliary heaters (10 in each drift) are treated individually as finite line sources with appropriate power tables. Because of the simplicity of the formulation, details of the emplacement borehole environment are not considered.

To approximate the effects of ventilation, line sources were positioned near the axial centerline of each drift. By assigning negative source strengths to these line sources, we were able to approximate the removal of heat by the ventilation airstream.

This model was implemented with STALKS, one of the PLUS family of codes (Montan, 1986). These codes automate the use of closed-form solutions for point, line, and planar sources in an infinite medium.

4 COMPARISONS OF DATA AND MODELING RESULTS

We compare modeling results with temperatures measured throughout the SFT-C facility for two purposes. First, such comparisons allow a direct assessment of the influence of each of several heat-transfer parameters on the calculational results. Because the SFT-C represents a large volume in which the heat flow has all the complexities of conductive, radiative, and convective heat transfer and ventilation, this aspect is essential. Second, it allows us to judge the adequacy of the three classes of heat-transfer models used in this study.

4.1 INFINITE-ARRAY FINITE-DIFFERENCE MODEL

As described above, the workhorse for both the pretest and posttest calculations was a two-dimensional infinite-length representation of the SFT-C array. We performed a series of eight calculations using this basic geometry and its associated finite-difference mesh representation. Table 5 summarizes the pertinent input parameters and conditions used in these calculations.

Table 5. Summary input parameters and conditions used in calculations.

Parameter	Calculation number					
	1148	1194[a]	1196	1197	1200	1201
Conductivity (W/m•K)	3.11	3.11	6.22	3.11	3.11	3.11
Capacity (J/kg•K)	930	930	930	930	930	1860
Ventilation ($m^3/s•m$)	0.026	0.026	0.026	0.006	0.026	0.026
Ambient rock temp. (C)	23	24.7	24.7	24.7	24.7	24.7
Inlet air temp. (C)	23	Meas.	Meas.	Meas.	Meas.	Meas.
Convection coefficient (Nusselt number, $\underline{R}_a$)	0.13	0.13	0.13	0.13	0.065	0.13

[a]1195: Conductivity = 3.42 W/m•K, otherwise like 1194. 1199: Low conductivity for walls and floor, otherwise like 1194. (Approximately 50% of normal over distances of 0.05 to 0.25 m.)

To examine the various effects we compared measured and calculated results. The three types of comparisons are temperature histories at selected locations, contours of calculated temperatures with measured temperatures superimposed at selected times, and cross-plots of measured and calculated temperatures at all instrumented locations in the mesh at selected times. Complete sets of the latter two types of data presentations are given in Appendices A and B, respectively.

4.1.1 Baseline Calculations

Calculation number 1148 (CN1148), the pretest design calculation reported by Montan and Patrick (1981), used the thermal properties, ventilation flow rate, ambient rock temperature, constant inlet air temperature, and convection coefficient selected before heated-phase testing was begun at the SFT-C. Plots of measured and calculated temperatures as a function of time allow us to examine the quality of this calculation at selected near-field locations. The positions chosen for all these comparisons are the canister, the liner, and rock at radial distances of 200 and 360 mm from the borehole wall of the center spent-fuel assembly (CEH09). Comparisons are made at three axial positions: 0.3 m below the top, the center, and 0.3 m above the bottom of the fuel assembly.

Although calculated temperatures are in excellent agreement with measurements at the center of the heated section, the calculation is uniformly low 3 m below the top and uniformly high 3 m above the bottom (Fig. 10). This suggests that the near-field model for convective heat transfer within the air-filled annular spaces may not be sufficiently accurate. Also, note that the calculation did not include the cooling phase and, hence, does not track the rapid decreases in temperature beyond 5.3 YOC.

Figures 11 and 12 allow us to compare measured and calculated temperature increases at all positions where temperatures were measured. The station designations of 2+83 and 3+45 refer to the heavily instrumented sections near the center and at the farther third-point of the test array, respectively (Fig. 3). As indicated by the near-unity slopes (A1), high R^2 (RR) values, and relatively small intercepts (A0) and mean-square errors (RM), data and calculation agree quite well throughout the test array. While it appears that the fit is better at station 3+45, we see that the data are consistently cooler than the calculation (as evidenced by the slope value of 0.9). A plausible explanation is that end effects begin to

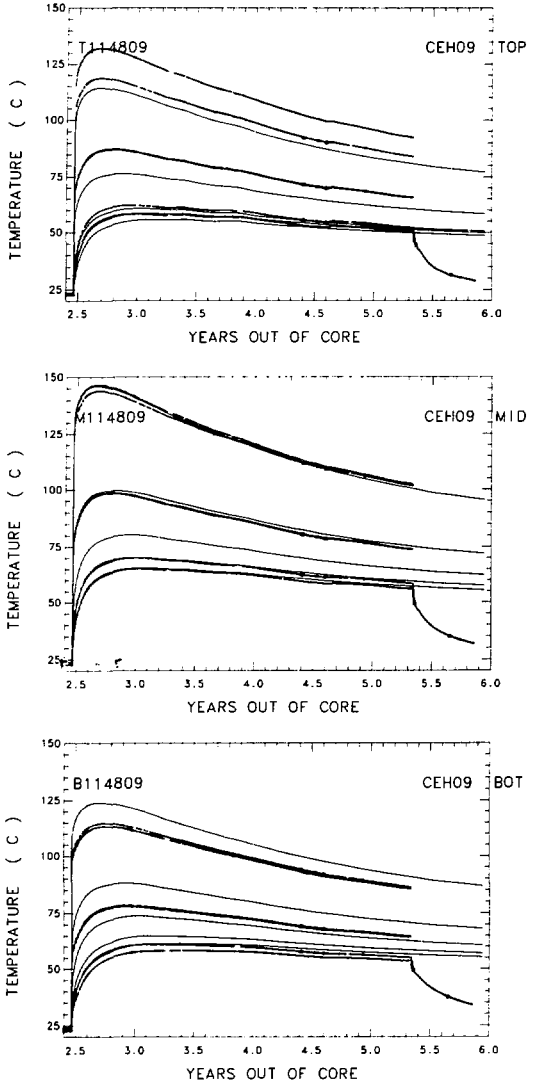

Figure 10. Comparison of measured and calculated near-field temperature histories, CN1148. (See text for discussion of measurement locations.)

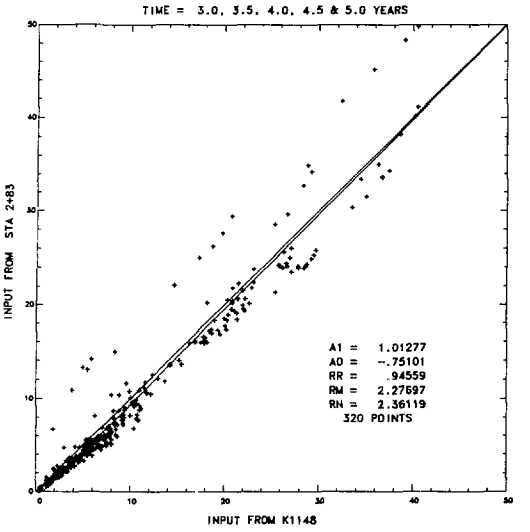

Figure 11. Cross plot of temperature increases measured at station 2+83 and calculated by CN1148.

influence the data at this location. Although the calculations assume an infinite-length array, these measurements are only about 10 m from the end of the array.

4.1.2 Initial Rock Temperature

For CN1194, we used a somewhat higher ambient rock temperature (as established by in situ measurements) and drove the ventilation model with the measured inlet-air temperature history. We also included ventilation to cool the rock mass during the construction phase of the experiment. This caused temperatures near the drifts to be cooler than the original 24.7C ambient at the start of the heated phase.

This calculation shows a similar high-quality comparison with the data (Fig. 13). In addition, we have captured the cooling response of the near field. With the exception of this very important addition, we see relatively minor improvements in the statistical measures of the fit between measured and

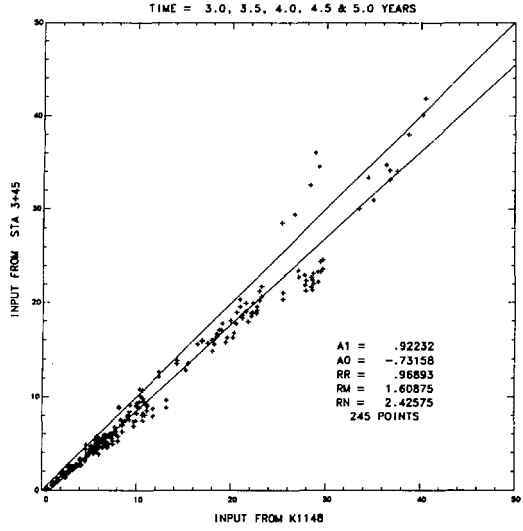

Figure 12. Cross plot of temperature increases measured at station 3+45 and calculated by CN1148.

calculated temperature changes (Figs. 14 and 15). As noted in Table 5, CN1194 also incorporated a higher ambient rock temperature and the measured inlet air temperature history. These changes produced somewhat better agreement between measured and calculated temperatures, particularly at early times (Appendix B, Figs. 11 through 22). This calculation appears to offer the best comparison with the test data.

4.1.3 Thermal Conductivity

The next three modifications allowed us to examine the effect of variations in thermal conductivity on the quality of the results. CN1195 and CN1196 used rock mass conductivities of 3.42 and 6.22 W/m•K, respectively, and CN1199 decreased the conductivity of a thin zone of rock near the surface of the drifts while maintaining the rock mass conductivity of 3.11 W/m•K.

The relatively modest 10% change in thermal conductivity produced equally modest differences in the calculated results. Examining Fig. 16, we see that

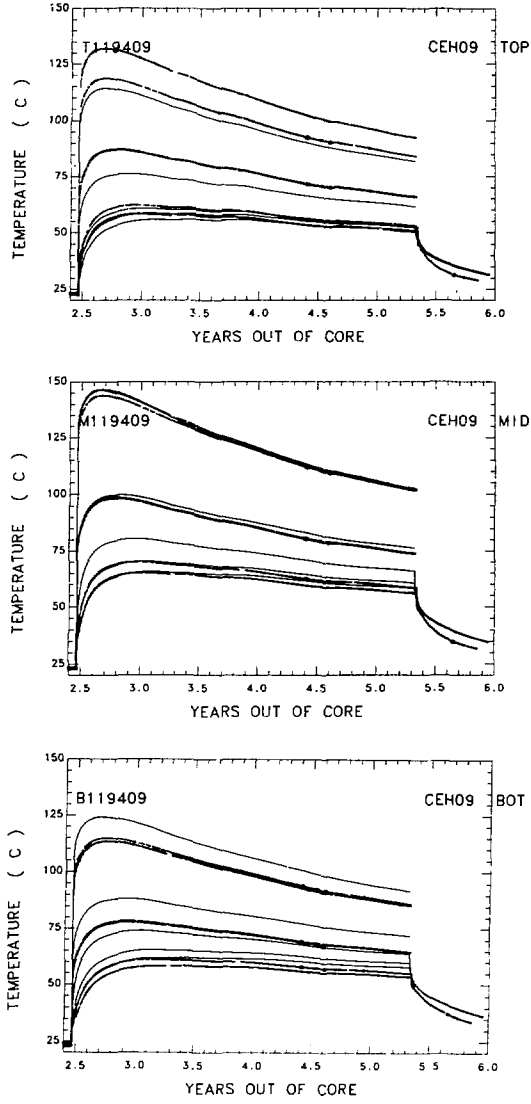

Figure 13. Comparison of measured and calculated near-field temperature histories, CN1194.

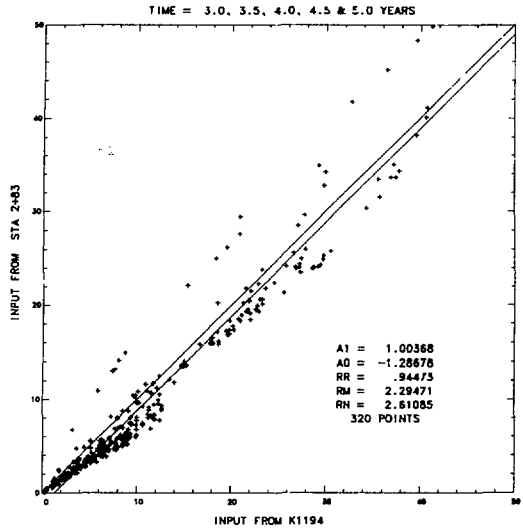

Figure 14. Cross-plot of temperature increases measured at station 2+83 and calculated by CN1194.

calculated temperatures decreased slightly in the near field, in comparison with CN1194. This produced a slight improvement in agreement at the borehole liner at all times as well as in the rock during the cooling period. Although the quality of the fit is basically unchanged, the slopes are uniformly high and the intercepts more negative at all times and locations (Appendix B, Figs. 23-24). This is a direct result of the lower near-field temperatures and higher far-field temperatures that occur because of the higher thermal conductivity.

As anticipated, the calculation for two-fold increase in conductivity (CN1196) produced substantially poorer results (Fig. 17). In addition to the generally poorer agreement between measured and calculated temperature changes (as evidenced by slopes of 1.5 or greater), the quality of the fit decreased considerably (Appendix B, Figs. 35 through 46).

CN1199 treated possible decreases in thermal conductivity in the rock immediately adjacent to the underground openings. Such decreases could result

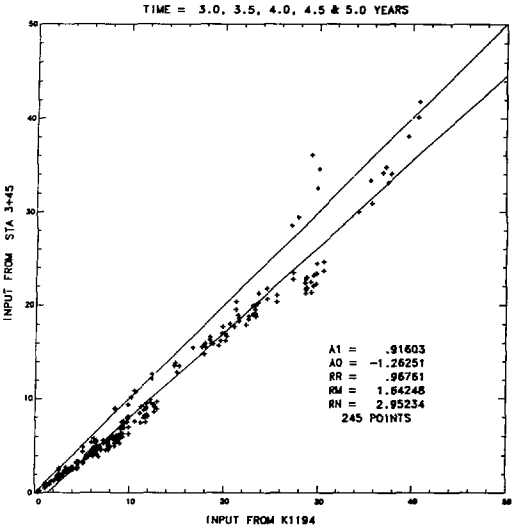

Figure 15. Cross-plot of temperature increases measured at station 3+45 and calculated by CN1194.

from excavation-induced fracturing of the rock. All other conditions and properties were the same as CN1194.

Incorporating lower thermal-conductivity zones near the drift surfaces produced subtle but conceptually important changes in the agreement between measured and calculated temperatures (Fig. 18). Because upward heat flow into the drifts was impeded, the calculated near-field temperatures increased slightly, producing somewhat better agreement between measured and calculated temperatures near the top of the heat source. Overall agreement between temperature changes was about as good as for CN1194 with somewhat flatter slopes seen for CN1199--a result of higher calculated temperatures (Figs. 19 and 20). The quality of the fit was essentially the same at all times during the test (Appendix B, Figs. 59 through 70).

4.1.4 Ventilation Effects

Despite the good agreement observed between the data and CN1194, examination of energy removal shows that the ventilation model does not agree

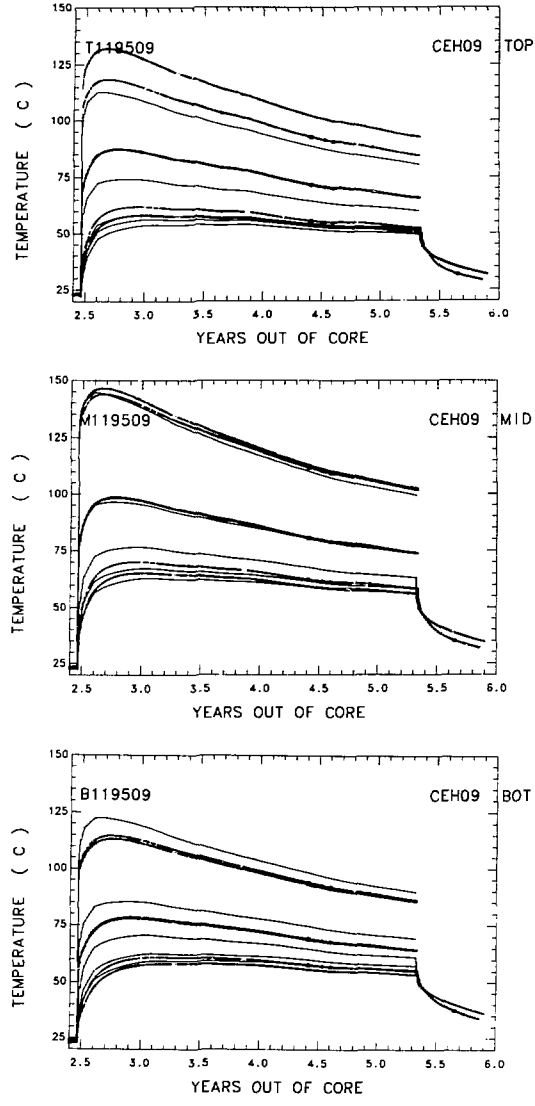

Figure 16. Comparison of measured and calculated near-field temperature histories, CN1195.

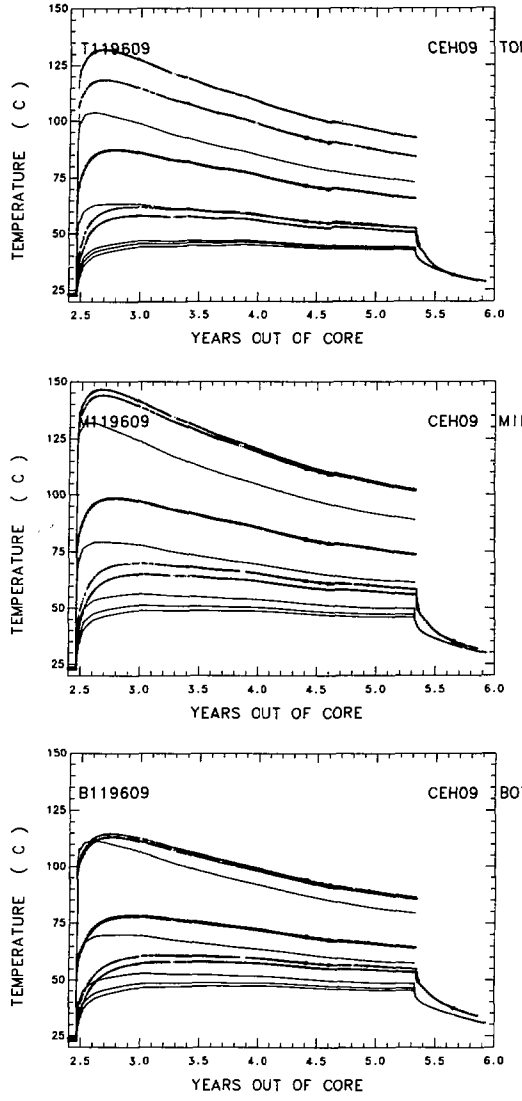

Figure 17. Comparison of measured and calculated near-field temperature histories, CN1196.

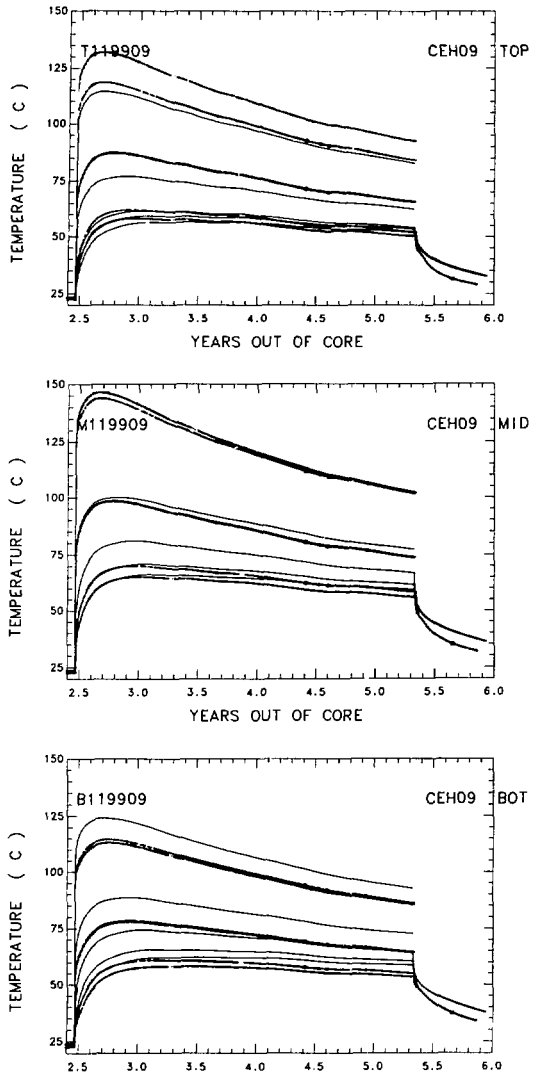

Figure 18. Comparison of measured and calculated near-field temperature histories, CN1199.

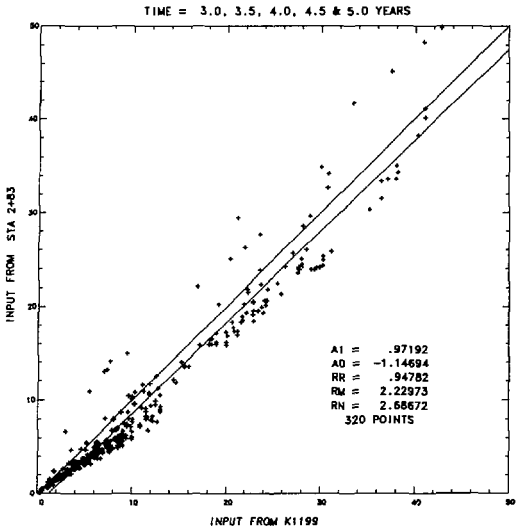

Figure 19. Cross-plot of temperature increases measured at station 2+83 and calculated by CN1199.

in either form or magnitude with the data recorded during the SFT-C. As indicated in Fig. 21, the TRUMP partial-flow model removed a steadily increasing quantity of energy beginning at 2.5 YOC, the time of initial emplacement. (Note that the modeled energy removal between 1.0 and 2.5 YOC occurred during construction and was not measured.) The data indicate a steady removal of energy with expected variations resulting from short-term changes in the ventilation flow rate. This discrepancy was observed early in the test (Patrick et al., 1982) and despite many attempts has not been resolved. Analyses indicate that the observed differences are much larger than could be attributed to instrumentation errors (Patrick et al., 1984b).

The effects of changes in ventilation flow rate were examined in CN1197. When preliminary calculations proved to be relatively insensitive to changes in flow rate, we introduced an approximate four-fold decrease (to reflect the average measured energy removal rate from the SFT-C) to examine this effect. The transfer of thermal energy to the ventilation airstream was also investigated in CN1200 by reducing the convection coefficient by a factor of 2.

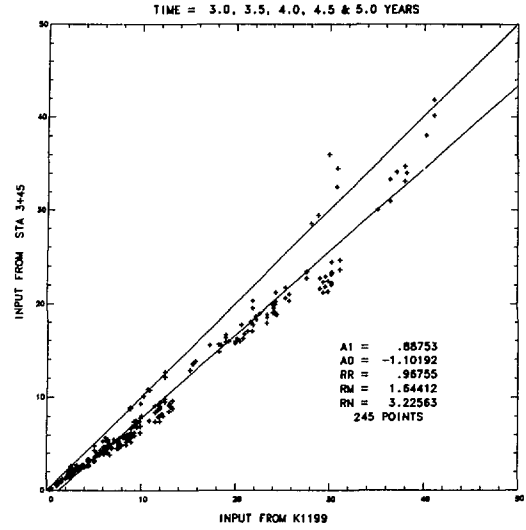

Figure 20. Cross-plot of temperature increases measured at station 3+45 and calculated by CN1199.

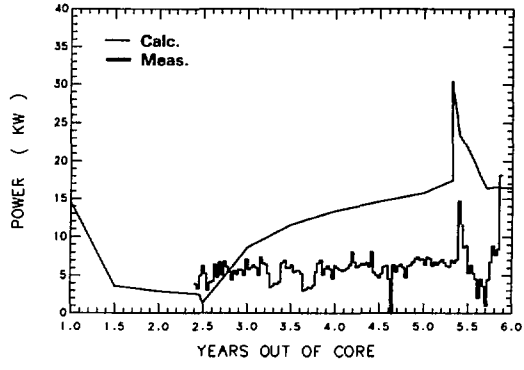

Figure 21. Comparison of energy removal rates measured and calculated by an infinite-length finite-difference representation of the SFT-C.

The four-fold decrease in flow rate produced poorer agreement at most near-field positions, particularly at later times (Fig. 22). It is particularly interesting that the measured and calculated temperature histories cross (in marked contrast to CN1148 and CN1194), indicating that the curves will eventually diverge widely. Overall, we see a slightly flatter slope and somewhat poorer fit between measured and calculated temperature changes (Appendix B, Figs. 47 through 58). These results indicate that the calculations are sensitive to flow rate and further indicate that the flow rate used in CN1194 is more nearly correct.

The change in convection coefficient subtly reduced the rate of removal of energy; this effect is similar to the influence of decreased flow rate. However, the agreement between measured and calculated temperatures appears to be essentially unchanged, indicating the relative insensitivity of the results to changes in convection coefficient (Fig. 23). Examination of the cross-plots confirms this observation (Appendix B, Figs. 71 through 82): the slopes and intercepts are only slightly different and the fit is slightly poorer for CN1200 than for CN1194.

4.1.5 Heat Capacity

Finally, we doubled the mass heat capacity in CN1201 to investigate the sensitivity of results to this property. The effect was relatively small in the near-field environment (Fig. 24). In general, we see that the calculated temperatures are uniformly lower than they were in CN1194, an anticipated result. These changes are on the order of 5C or less in the canister region. An examination of the cross-plots indicates that the effect throughout the array is to decrease the calculated temperatures (Appendix B, Figs. 83 through 94), increasing the slopes and decreasing the intercepts. The fits are about as good as for CN1194. These observations indicate the relative insensitivity of the results to the selected value of heat capacity.

4.2 FINITE-ARRAY FINITE-DIFFERENCE MODEL

Similar but less extensive comparisons may be made between measured temperatures and those calculated with the fully three-dimensional finite-length array model of the SFT-C. Calculation number 1193 represents our initial effort to model the true three-dimensional finite-length geometry of the SFT-C.

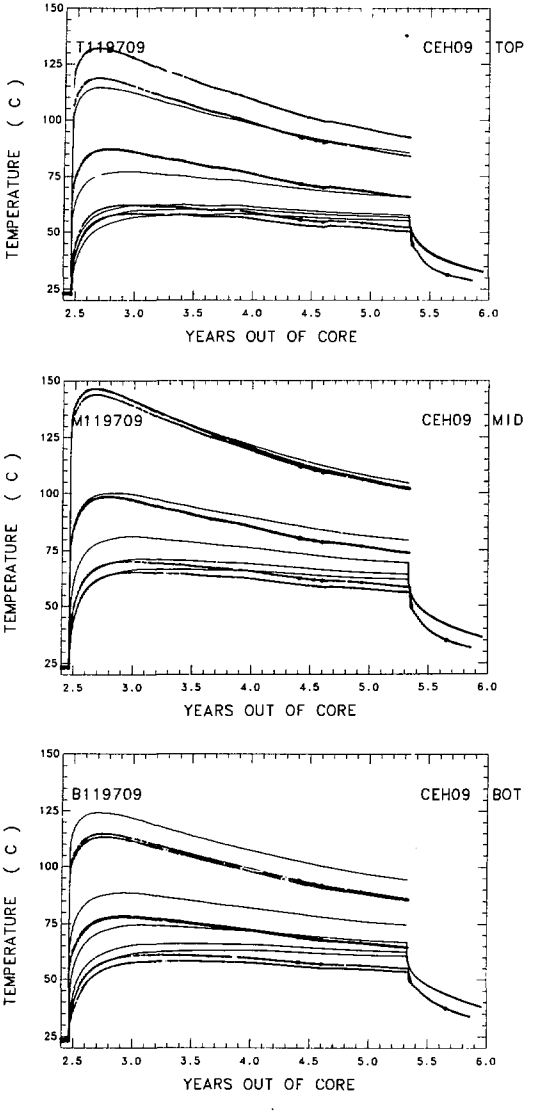

Figure 22. Comparison of measured and calculated near-field temperature histories, CN1197.

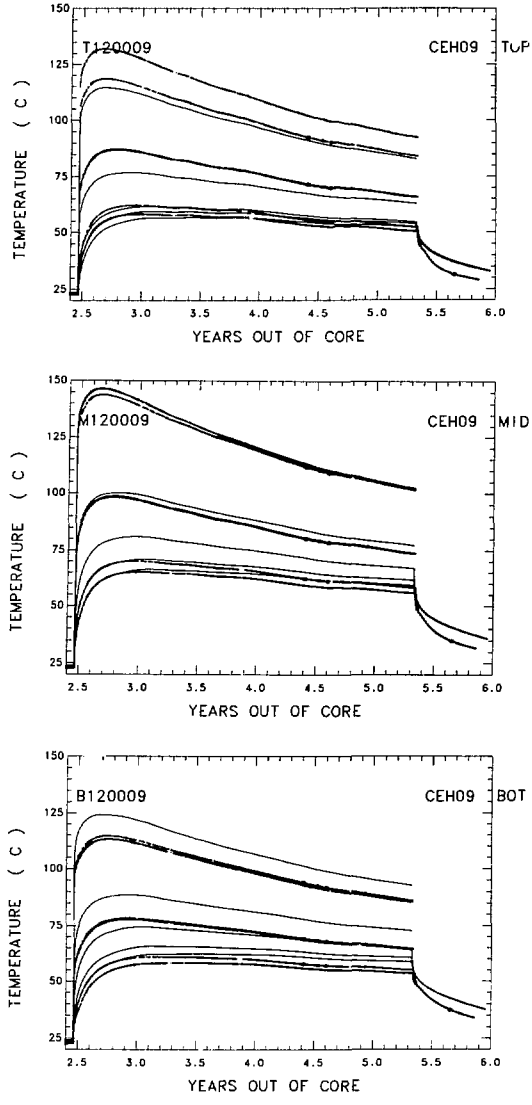

Figure 23. Comparison of measured and calculated near-field temperature histories, CN1200.

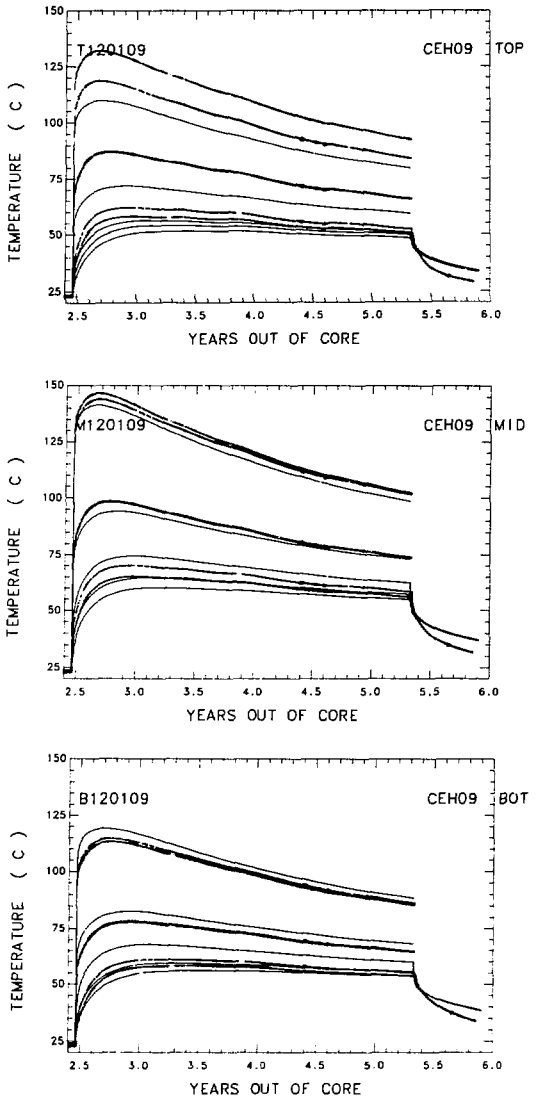

Figure 24. Comparison of measured and calculated near-field temperature histories CN1201.

4.2.1 Rock Temperatures

The results of this first effort were excellent. Although we believe the infinite-array model gave adequate results, the results of the finite-length model were remarkably better. In addition to the anticipated improvements near the ends of the SFT-C array, we also saw improvements near the center of the array for points near the drift surfaces. We discuss each of these improvements here, using CN1194 (our best infinite-length model) as a basis of comparison.

The anticipated improvement near the ends of the array is seen clearly in Figs. 25 and 26, which show measured and calculated temperatures 2.1 and 13.3 m below the floor of the emplacement drift (respectively) and about 2.0 m from drift centerline. In the left half of the former figure, the calculation produces a rapid rise in temperature at about 2.5 YOC (when the spent-fuel was emplaced) and a similar decrease upon retrieval at 5.3 YOC. This models the response of an infinite array. The right section of Fig. 25 shows the smaller-magnitude thermal pulse for instrument AET011, which was located more than 6 m from the last spent-fuel emplacement hole. Agreement between the finite-array calculational result and the data is excellent. A similar effect is seen for the position 13.3 m below the drift surface (Fig. 26). These results indicate that the finite-length model much more accurately reflects in situ heat flow near the ends of the test array.

Significant, if unexpected, improvements were observed near the central regions of the test array. Figure 27 shows that CN1194 tended to overestimate

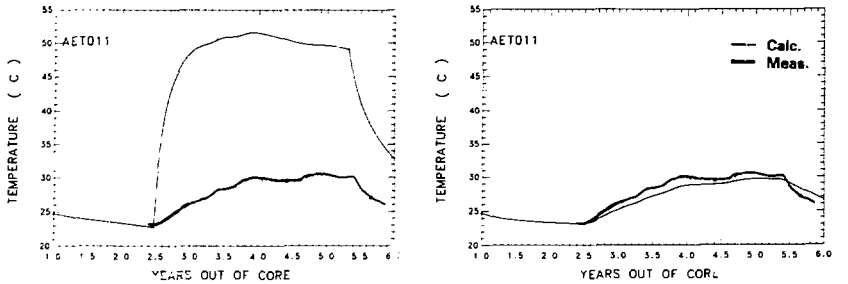

Figure 25. Measured and calculated temperature histories at a position 2.1 m below the floor near the end of the SFT-C array. The left figure is the infinite-length model and the right figure is the finite-length model.

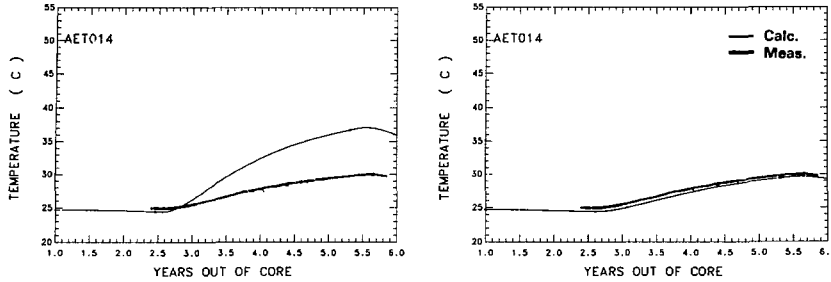

Figure 26. Measured and calculated temperature histories at a position 13.3 m below the floor near the end of the SFT-C array. The left figure is the infinite-length model and the right figure is the finite-length model.

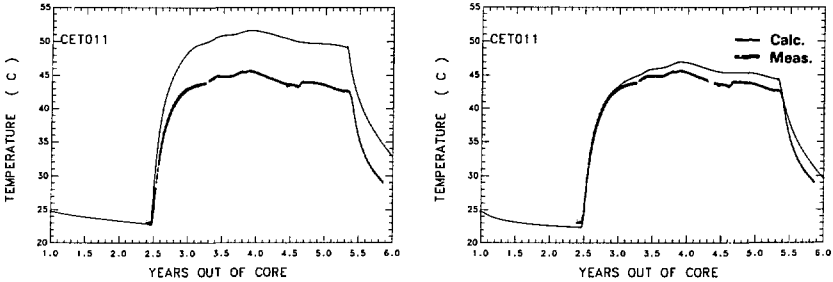

Figure 27. Measured and calculated temperature histories at a position 2.0 m below the floor near the center of the SFT-C array. The left figure is the infinite-length model and the right figure is the finite-length model.

temperatures at instrument CET011 by 5 to 8C. Since CN1194 was positioned 1.8 m laterally from the canister drift centerline and 2 m below the drift floor near the center emplacement borehole, one would have expected reasonably good agreement with the data. We see that the finite-length array model provides considerably better agreement. Similar results may be seen in the center (Fig. 28), above (Fig. 29), and beneath the pillar, midway between the linear arrays of heat sources (Fig. 30). In all cases, the finite-length model produces cooler temperatures than its infinite-length counterpart.

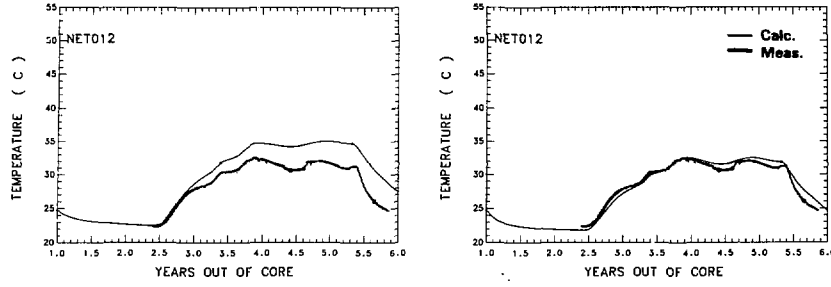

Figure 28. Measured and calculated temperature histories at a position near the center of the pillar between the two drifts. The left figure is the infinite-length model and the right figure is the finite-length model.

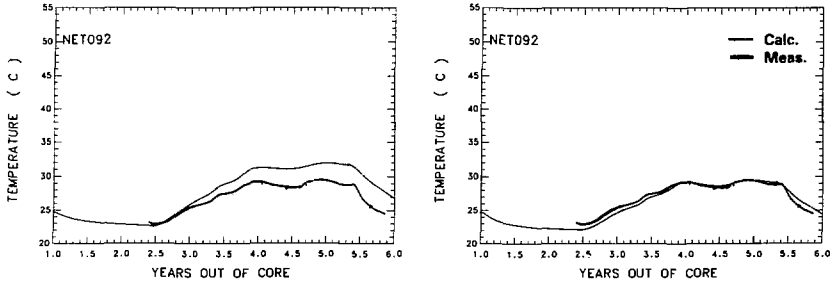

Figure 29. Measured and calculated temperature histories at a position near the center and above the pillar between the two drifts. The left figure is the infinite-length model and the right figure is the finite-length model.

4.2.2 Ventilation Effects

A plausible explanation for the improved agreement between measured and calculated rock temperatures near the center of the SFT-C may be found in differences in the ventilation models. In Fig. 31, we see that the ventilation model for the finite-length array removed somewhat more energy than did the counterpart model used in CN1194 (Fig. 21). The removal of additional heat resulted directly in lower calculated temperatures.

This removal of additional heat is believed to result from differences in the two ventilation models. Although we were able to treat ventilation and related convective and radiative heat processes in considerable detail in the

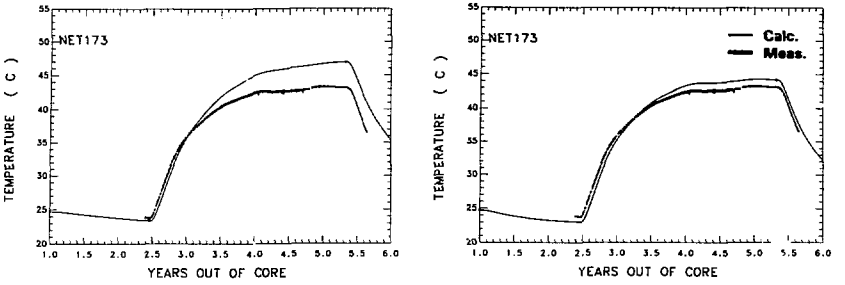

Figure 30. Measured and calculated temperature histories at a position 4.8 m below the pillar, midway between the center and north heater drifts. The left figure is the infinite-length model and the right figure is the finite-length model.

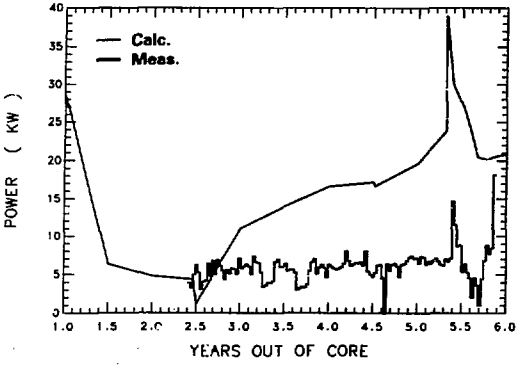

Figure 31. Comparison of rates of energy removal measured and calculated by a finite-length, finite-difference model of the SFT-C.

infinite-length model, computational limitations constrained us to simplify the finite-length model. The latter model treated the air in the drifts as a highly conductive solid, with central nodes in the drifts connected to external nodes via heat-transfer coefficients. Since these external nodes were regulated to match the measured inlet-air temperature histories, they caused heat to flow out of the calculational mesh, simulating ventilation.

With a model of this type, the temperatures near the drift surfaces were lower than those for the model that incorporated thermal radiation.

4.3 FINITE-ARRAY ANALYTICAL MODEL

Results from the finite-array analytical model may also be compared with measured temperatures to assess the adequacy of such relatively simple models. As previously discussed, the ventilation process was approximated by "negative sources" positioned in each of the three drifts. Initial calculations with a power-removal history approximating the measured history were not too successful (Fig. 32). As one might expect from the results of the other models, more heat must be removed by the calculation than was measured to be removed. Figure 33 displays a typical example of how the calculated temperatures increase more rapidly and continue to diverge from the measurements during the heated phase of the test.

A second calculation quadrupled the energy-removal rate to simplistically approximate the higher rate of removal observed in the TRUMP calculations (Fig. 34). As expected, very good results were achieved. Examination of Fig. 35 indicates that the level of agreement is nearly as good as was obtained with the finite-length TRUMP model. Looking further, we see

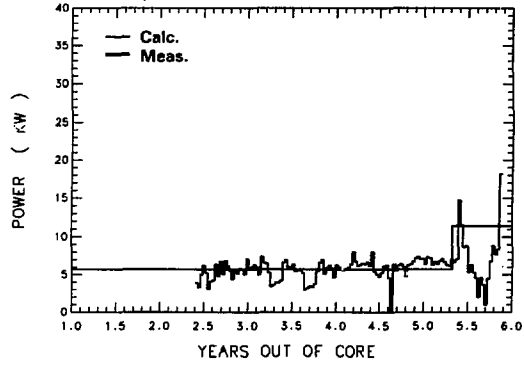

Figure 32. Approximation of energy removal rate used in an analytical model of the SFT-C compared with measured removal rate.

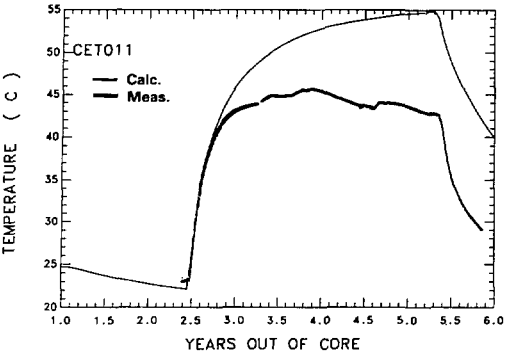

Figure 33. Measured and calculated temperature histories at a position 2.0 m below the floor near the center of the SFT-C array. Calculated values are from a three-dimensional analytical solution with the energy removal rate about equal to the measured value.

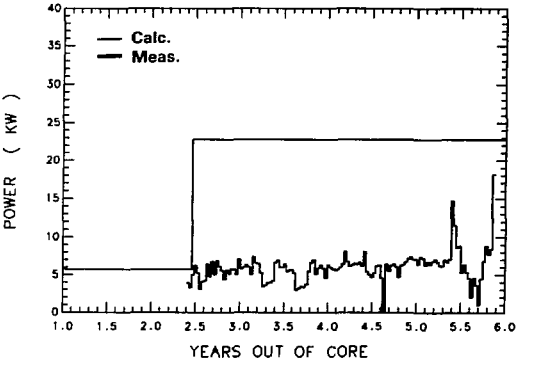

Figure 34. Approximation of four times the measured energy removal rate, as used in an analytical model of the SFT-C, compared with the measured removal rate.

that this is not the case at all locations. Near the drifts, the STALKS calculations tend to substantially underestimate the temperatures (Fig. 36). This is a direct result of these points being sufficiently close to the heat sink that their temperatures are adversely affected.

Even though quite good agreement was obtained using this simplistic model, two important items must be considered before applying it to future designs. First, the energy removal rate must be known before the model can be used. Furthermore, it may be necessary to apply some factor (as in this case) to obtain realistic results. Second, this model cannot provide details of heat flow near emplacement boreholes or similar locations that may be of interest to the test or repository designer.

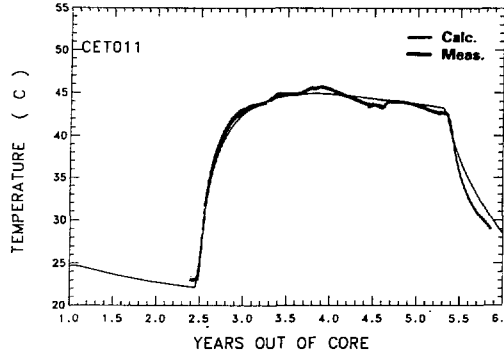

Figure 35. Measured and calculated temperature histories at a position 2.0 m below the floor near the center of the SFT-C array. Calculated values are from a three-dimensional analytical solution with the energy removal rate about four times the measured value.

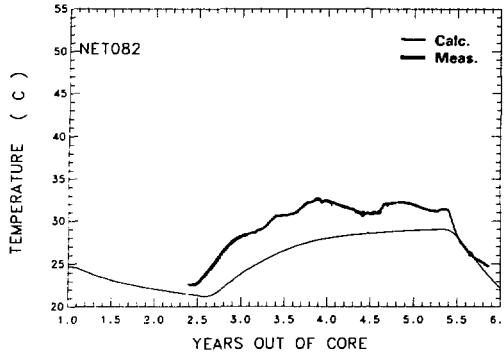

Figure 36. Measured and calculated temperature histories at a position near the center of the pillar between the two drifts. Calculated values are from a three-dimensional analytical solution with the energy removal rate about four times the measured value.

5 SUMMARY AND CONCLUSIONS

From the development of the original test concept through detailed design and data analyses, heat transfer calculations have played an important role in the SFT-C. Following retrieval of spent fuel from the SFT-C, a final set of calculations was performed with the best available heat transfer properties, thermal source strengths, and ventilation parameters. Most of these calculations were done with the finite-difference code TRUMP, with the SFT-C modeled as one-quarter of a unit cell of an infinite-length repository. Additional calculations with TRUMP treated the test array in a fully three-dimensional finite-length model, and a finite-length three-dimensional model (with the PLUS family of analytical solutions) was also employed. In this simplified case, it was possible to treat only conductive heat-transfer processes. Thus, details of the spent-fuel storage configuration could not be modeled, and thermal radiation, convection, and ventilation processes were approximated by conductive processes and thermal sinks (in the case of ventilation).

Two notable improvements in the as-built calculation were achieved. First, efforts to improve the agreement between measured and calculated

intermediate-field temperatures were successful because we used better initial temperatures and accounted for cooling of the rock mass during construction. Second, our calculation of the post-retrieval cooling of the rock mass was also quite successful.

Attempts to improve upon our ability to model both the detailed axial heat distribution near the canisters and also the removal of thermal energy in the ventilation airstream were not successful. Capturing the near-field phenomena, even with a detailed three-dimensional model of the emplacement geometry, has been impossible. Even so, we believe that the errors observed indicate that the modeling is adequate for designing future tests and repositories.

Successful calculation of the ventilation process has been even more elusive. Although our measurements indicate a relatively constant energy-removal rate, our calculations (and theoretical considerations) suggest that the rate should increase fairly rapidly as initial heating takes place and then gradually increase throughout the test duration.

A series of eight infinite-length model TRUMP calculations indicated that the calculational results were quite insensitive to fairly wide variations in the basic thermal properties and the ventilation flow rate. These results suggest that reasonable estimates of these properties from laboratory testing, or in some cases handbook values, will provide calculational results that are adequate for most design purposes. Even our original calculations were within about 5 to 10°C of the measured values in the near-field canister environment.

A fully three-dimensional finite-length TRUMP model of the SFT-C produced excellent results, including marked improvements in two general areas. First, although the infinite-length model produced temperatures 20°C or more higher than measured near the ends of the drifts, the new model results were typically within 3°C of the data. This improvement is a direct result of treating heat flow out the ends of the array. Second, we also saw significant improvements at positions near the drift surfaces, in the pillar between drifts, and in the rock mass above and below the pillars. Since these latter improvements were observed near the central region of the SFT-C where the infinite-array model is known to accurately represent test conditions, we attribute them to the different ventilation model used in this calculation.

We obtained an analytical solution of the finite-length SFT-C array with the code STALKS, but found it necessary to arbitrarily increase the measured energy removal rate four-fold to obtain good results. It is interesting to

note that this increase approximates the rate of removal calculated by the finite-difference models. Rock temperatures calculated by this model were in very good agreement with measured values except where the measurements were close to the heat sinks used to remove energy from the problem. This observation suggests that a relatively simple heat-sink model may accurately represent energy removal in the ventilation airstream. However, one must know a priori the energy-removal rate to use this model effectively. Furthermore, a simple heat-sink model will not estimate the actual air temperature--a quantity often needed for examining the health and safety implications of a facility design.

6 ACKNOWLEDGMENTS

Overall guidance for this and other NNWSI projects at LLNL is provided by L. D. Ramspott. Special recognition is due him and L. B. Ballou who originated the idea of a spent-fuel test and provided leadership and technical expertise which led to the success of the test. In addition, we thank L. B. Ballou, F. E. Heuze, W. Stein, and J. L. Yow, Jr. for their careful reviews and helpful comments on this report.

7 BIBLIOGRAPHY

W. Brough and W. Patrick, Instrumentation Report #1: Specification, Design, Calibration, and Installation of Instrumentation for an Experimental, High Level, Nuclear Waste Storage Facility, Lawrence Livermore National Laboratory, Livermore, CA, UCRL-53248 (1982).

T. R. Butkovich and D. N. Montan, A Method for Calculating Internal Radiation and Ventilation with the ADINAT Heat-Flow Code, Lawrence Livermore National Laboratory, Livermore, CA, UCRL-52918 (1980).

A. L. Edwards, TRUMP, A Computer Program for Transient and Steady State Temperature Distribution in Multidimensional Systems, Lawrence Livermore National Laboratory, Livermore, CA, UCRL-14754, Rev. 3 (1972).

D. N. Montan, The PLUS Family, A Set of Computer Programs to Evaluate Analytical Solutions of the Diffusion Equation, Lawrence Livermore National Laboratory, Livermore, CA, UCID-20680 (1986).

D. N. Montan and W. E. Bradkin, Heater Test 1, Climax Stock Granite, Nevada, Lawrence Livermore National Laboratory, Livermore, CA, UCRL-53496 (1984).

D. Montan and W. Patrick, Thermal Calculations for the Design, Construction, Operation, and Evaluation of the Spent Fuel Test--Climax, Nevada Test Site, Lawrence Livermore National Laboratory, Livermore, CA, UCRL-53238 (1981).

W. C. Patrick, Spent-Fuel Test--Climax: An Evaluation of the Technical Feasibility of Geologic Storage of Spent Nuclear Fuel in Granite. Final Report, Lawrence Livermore National Laboratory, Livermore, CA, UCRL-53702 (1986).

W. C. Patrick, L. B. Ballou, T. R. Butkovich, R. C. Carlson, W. B. Durham, G. L. Hage, E. L. Majer, D. N. Montan, R. A. Nyholm, N. L. Rector, D. G. Wilder, and J. L. Yow, Jr., Spent Fuel Test-Climax: Technical Measurements Interim Report Fiscal Year 1981, Lawrence Livermore National Laboratory, Livermore, CA, UCRL-53294 (1982).

W. C. Patrick, L. B. Ballou, T. R. Butkovich, R. C. Carlson, W. B. Durham, G. L. Hage, E. L. Majer, D. N. Montan, R. A. Nyholm, N. L. Rector, D. G. Wilder, and J. L. Yow, Jr., Spent Fuel Test-Climax: Technical Measurements Interim Report Fiscal Year 1982, Lawrence Livermore National Laboratory, Livermore, CA, UCRL-53294-82 (1983).

W. C. Patrick, T. R. Butkovich, R. C. Carlson, W. B. Durham, H. C. Ganow, G. L. Hage, E. L. Majer, D. N. Montan, R. A. Nyholm, N. L. Rector, F. J. Ryerson, H. Weiss, and J. L. Yow, Jr., Spent Fuel Test-Climax: Technical Measurements Interim Report Fiscal Year 83, Lawrence Livermore National Laboratory, Livermore, CA, UCRL-53294-83 (1984a).

W. C. Patrick, N. L. Rector, and J. J. Scarafiotti, Instrumentation Report No. 3: Performance and Reliability of Instrumentation Deployed for the Spent Fuel Test-Climax, Lawrence Livermore National Laboratory, Livermore, CA, UCRL-53637 (1984b).

L. D. Ramspott, L. B. Ballou, R. C. Carlson, D. N. Montan, T. R. Butkovich, J. E. Duncan, W. C. Patrick, D. G. Wilder, W. G. Brough, and M. C. Mayr, Technical Concept for a Test of Geologic Storage of Spent Reactor Fuel in the Climax Granite, Nevada Test Site, Lawrence Livermore National Laboratory, Livermore, CA, UCRL-52796 (1979).

F. Schmittroth, G. J. Neely, and J. C. Krogness, A Comparison of Measured and Calculated Decay Heat for Spent Fuel Near 2.5 Years Cooling Time, Hanford Engineering Development Laboratory, Richland, WA, HEDL-7202 (1982).

D. G. Wilder and J. L. Yow, Jr., Structural Geology Report, Spent Fuel Test-Climax, Nevada Test Site, Lawrence Livermore National Laboratory, Livermore, CA, UCRL-53381 (1984).

MLD/BSS/NMS

APPENDIX A

CALCULATED TEMPERATURE CONTOURS AND MEASURED TEMPERATURES

CALCULATION NUMBER 1194

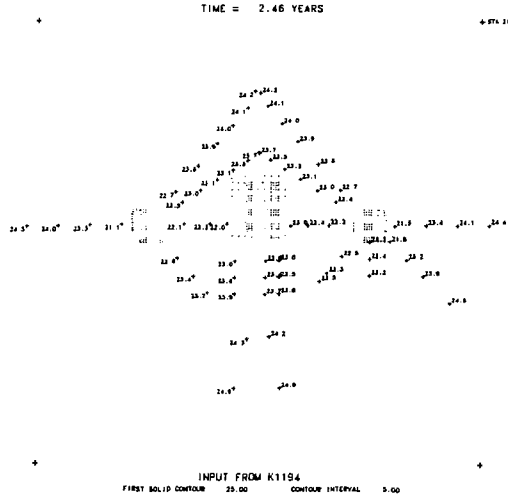

Figure A-1. Measured temperatures and contours of calculated temperatures at 2.46 YOC, station 2+83.

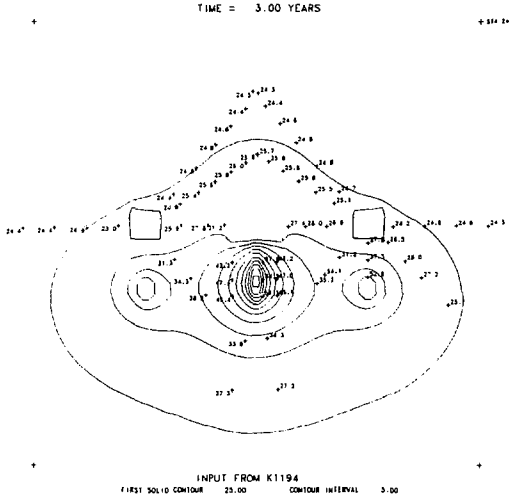

Figure A-2. Measured temperatures and contours of calculated temperatures at 3.00 YOC, station 2+83.

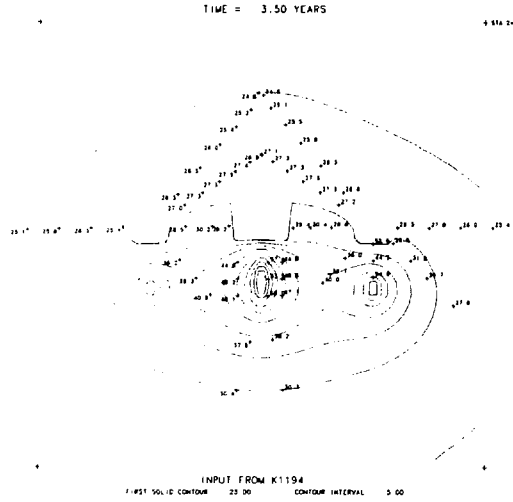

Figure A-3. Measured temperatures and contours of calculated temperatures at 3.50 YOC, station 2+83.

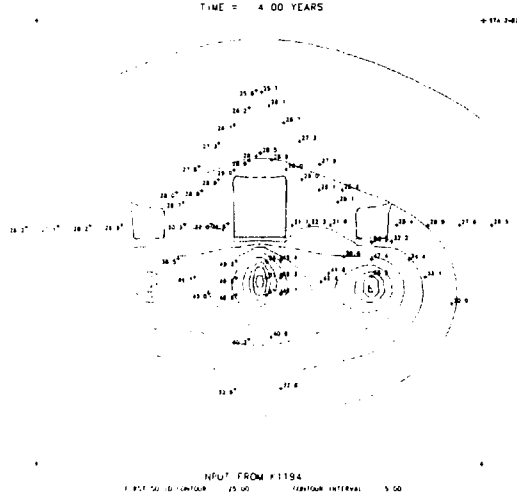

Figure A-4. Measured temperatures and contours of calculated temperatures at 4.00 YOC, station 2+83.

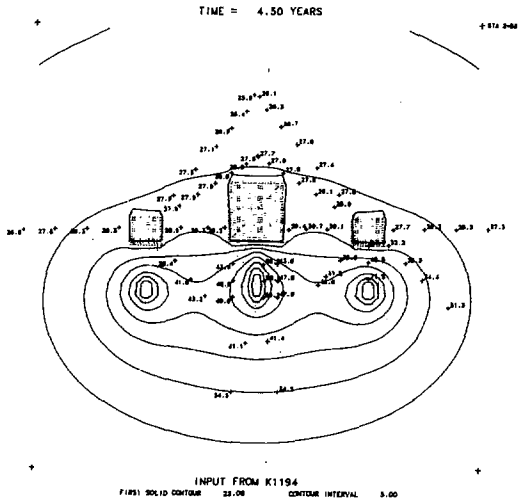

Figure A-5. Measured temperatures and contours of calculated temperatures at 4.50 YOC, station 2+83.

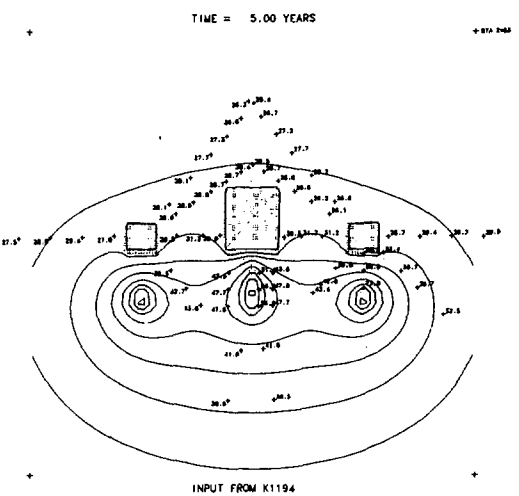

Figure A-6. Measured temperatures and contours of calculated temperatures at 5.00 YOC, station 2+83.

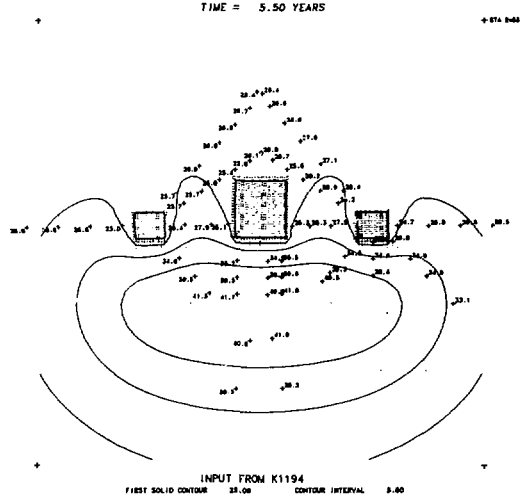

Figure A-7. Measured temperatures and contours of calculated temperatures at 5.50 YOC, station 2+83.

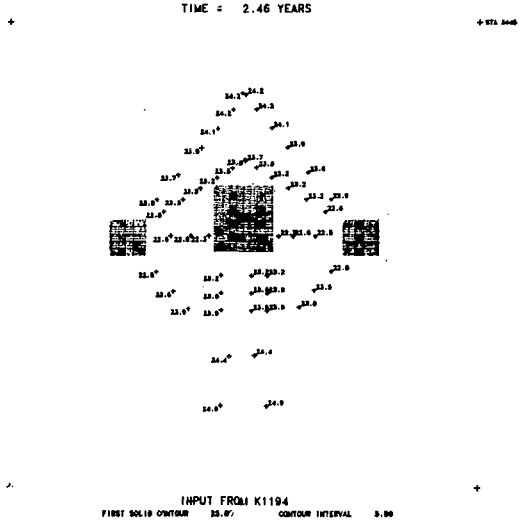

Figure A-8. Measured temperatures and contours of calculated temperatures at 2.46 YOC, station 3+45.

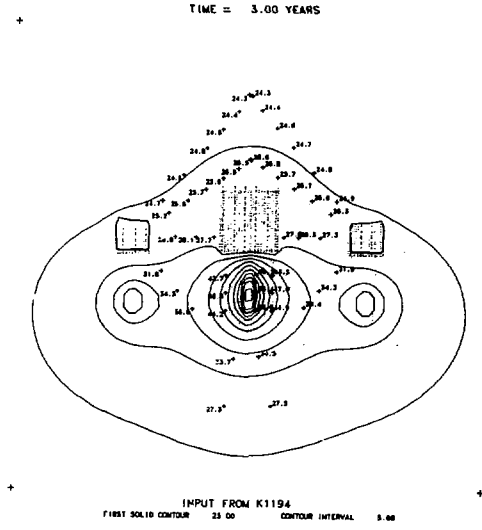

Figure A-9. Measured temperatures and contours of calculated temperatures at 3.00 YOC, station 3+45.

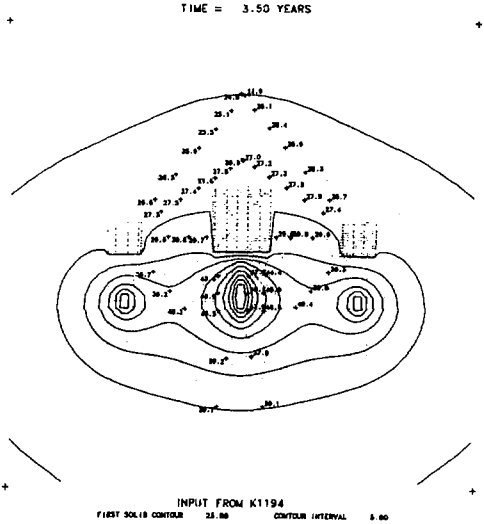

Figure A-10. Measured temperatures and contours of calculated temperatures at 3.50 YOC, station 3+45.

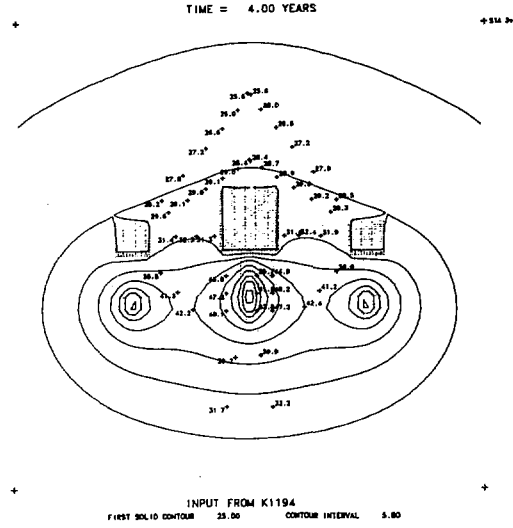

Figure A-11. Measured temperatures and contours of calculated temperatures at 4.00 YOC, station 3+45.

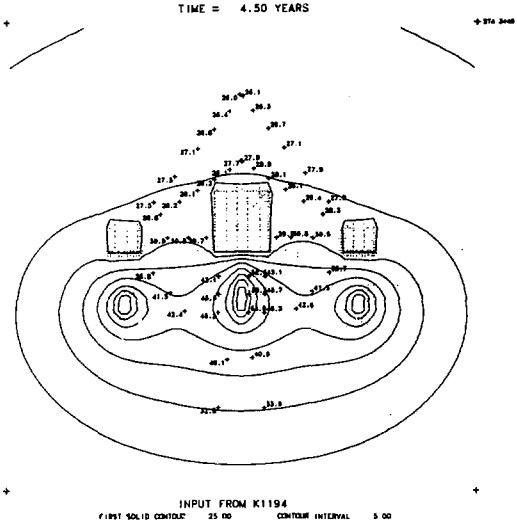

Figure A-12. Measured temperatures and contours of calculated temperatures at 4.50 YOC, station 3+45.

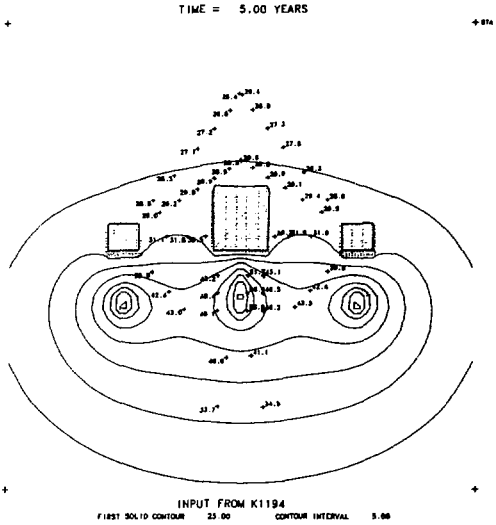

Figure A-13. Measured temperatures and contours of calculated temperatures at 5.00 YOC, station 3+45.

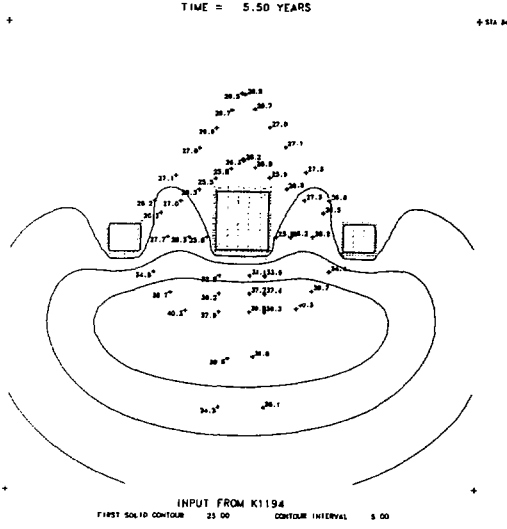

Figure A-14. Measured temperatures and contours of calculated temperatures at 5.50 YOC, station 3+45.

APPENDIX B

CROSS-PLOTS OF MEASURED AND CALCULATED

TEMPERATURE RISES ABOVE AMBIENT

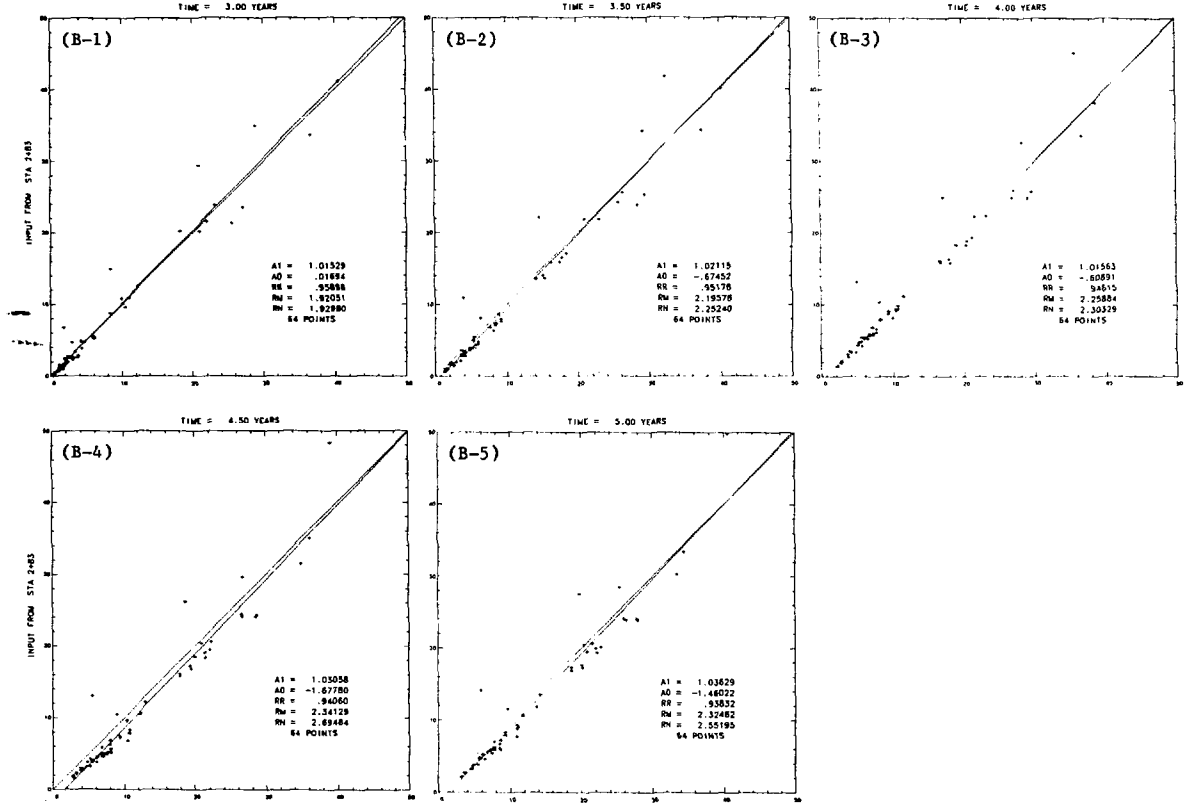

Figure B-1 through B-5. Measured vs calculated (CN1148) temperature rises at 3.00, 3.50, 4.00, 4.50, 5.00 YOC, station 2+83.

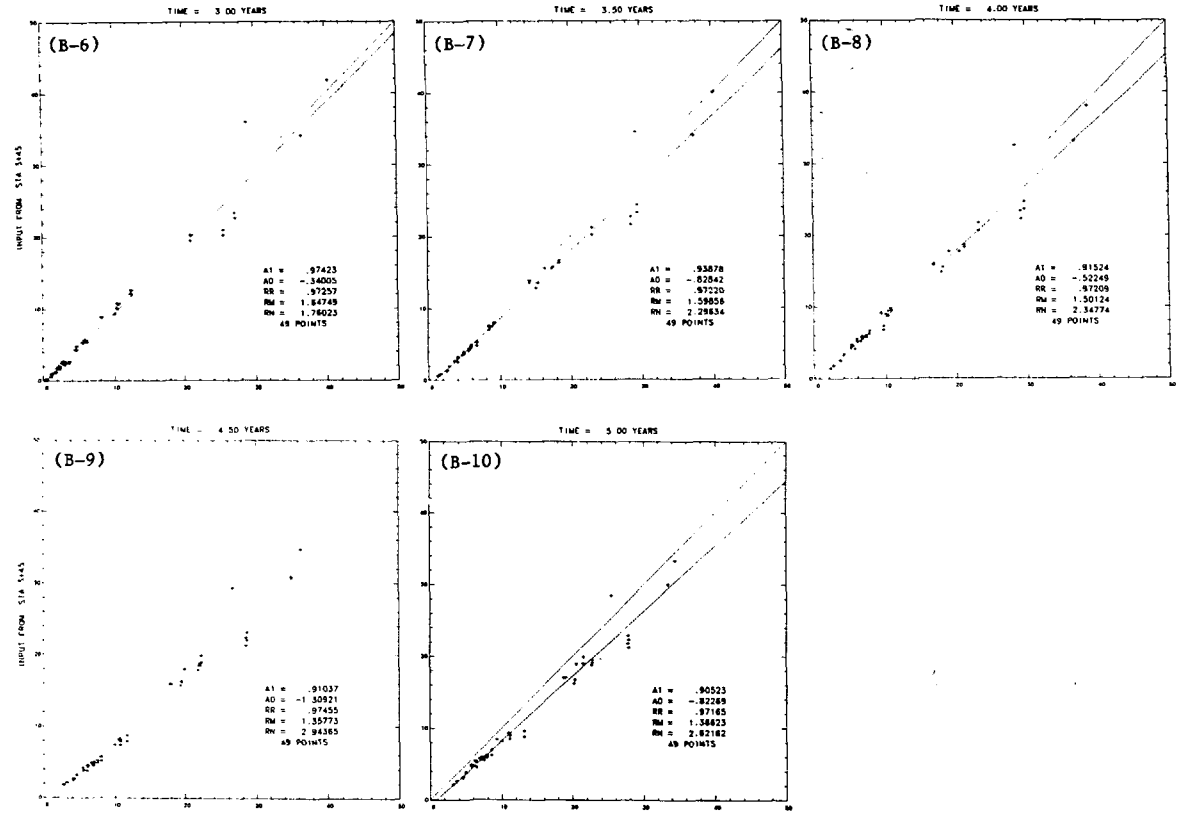

Figure B-6 through B-10. Measured vs calculated (CN1148) temperature rises at 3.00, 3.50, 4.00, 4.50, 5.00 YOC, station 3+45.

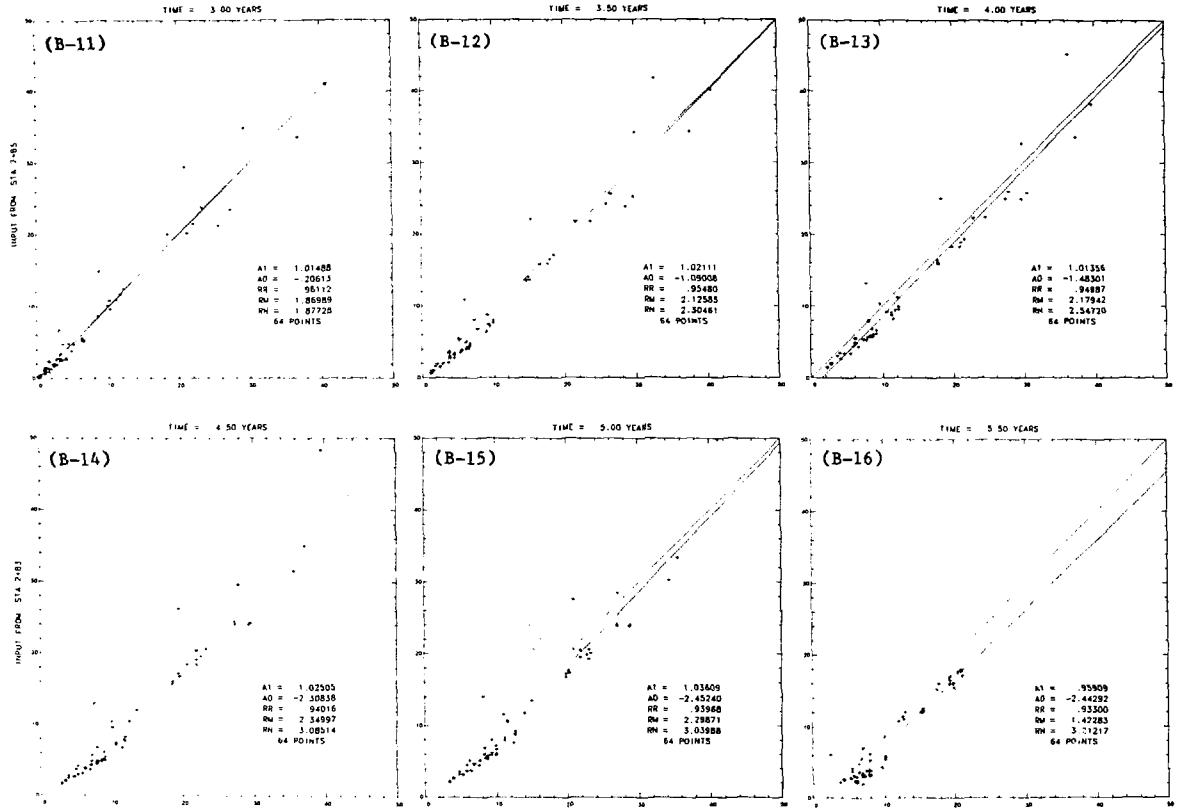

Figure B-11 through B-16. Measured vs calculated (CN1194) temperature rises at 3.00, 3.50, 4.00, 4.50, 5.00, 5.50 YOC, station 2+83.

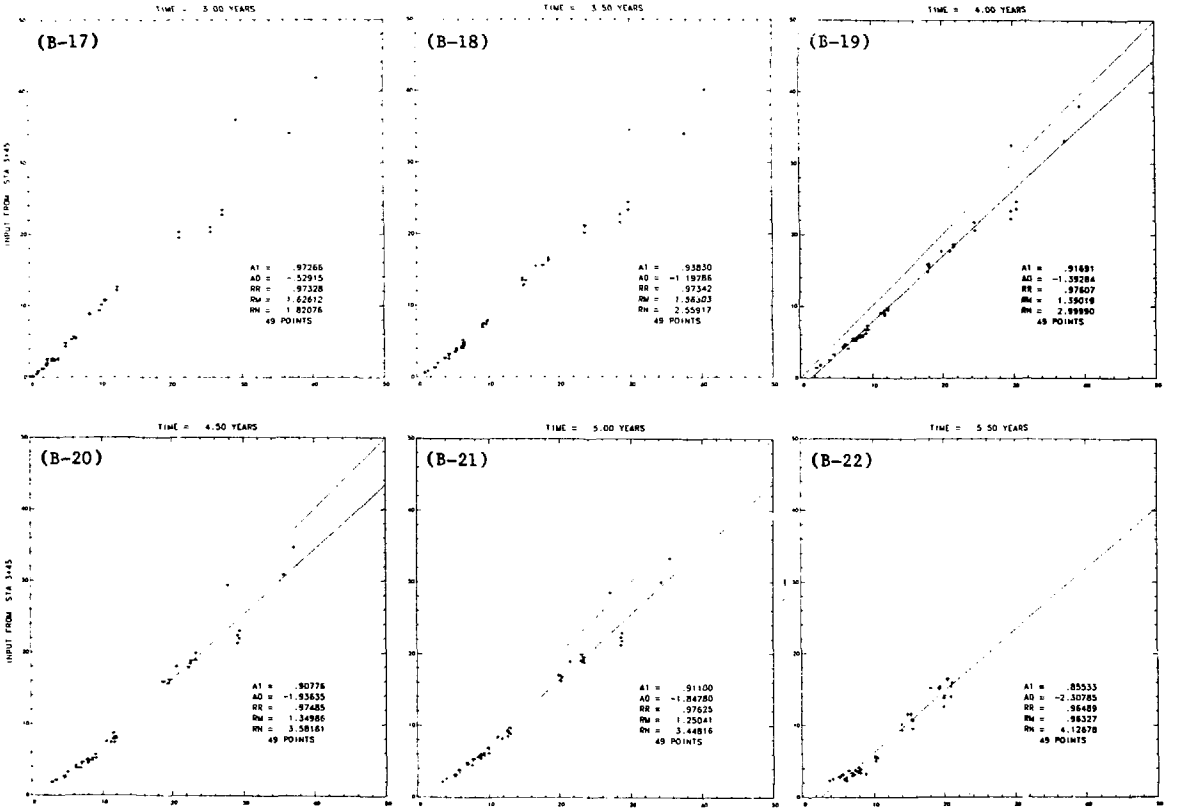

Figure B-17 through B-22. Measured vs calculated (CN1194) temperature rises at 3.00, 3.50, 4.00, 4.50, 5.00, 5.50 YOC, station 3+45.

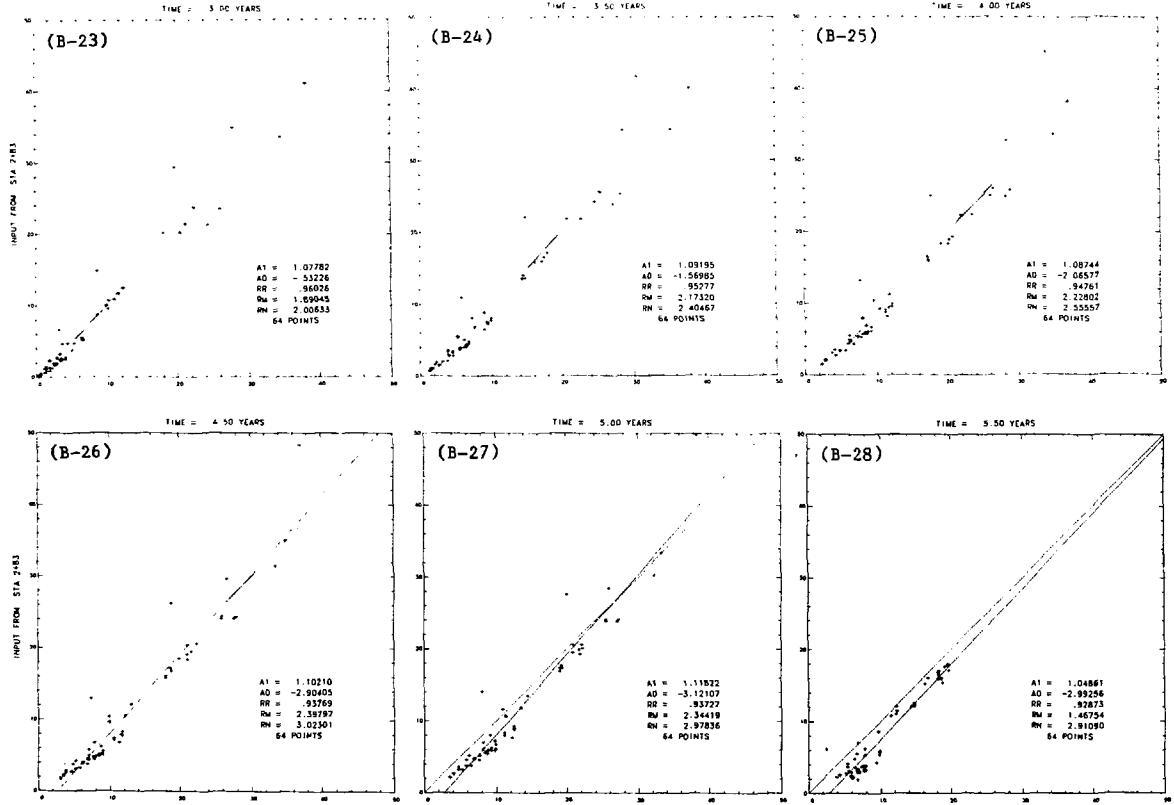

Fig. B-23 through B-28. Measured vs calculated (CN1195) temperature rises at 3.00, 3.50, 4.00, 4.50, 5.00, 5.50 YOC, station 2+83.

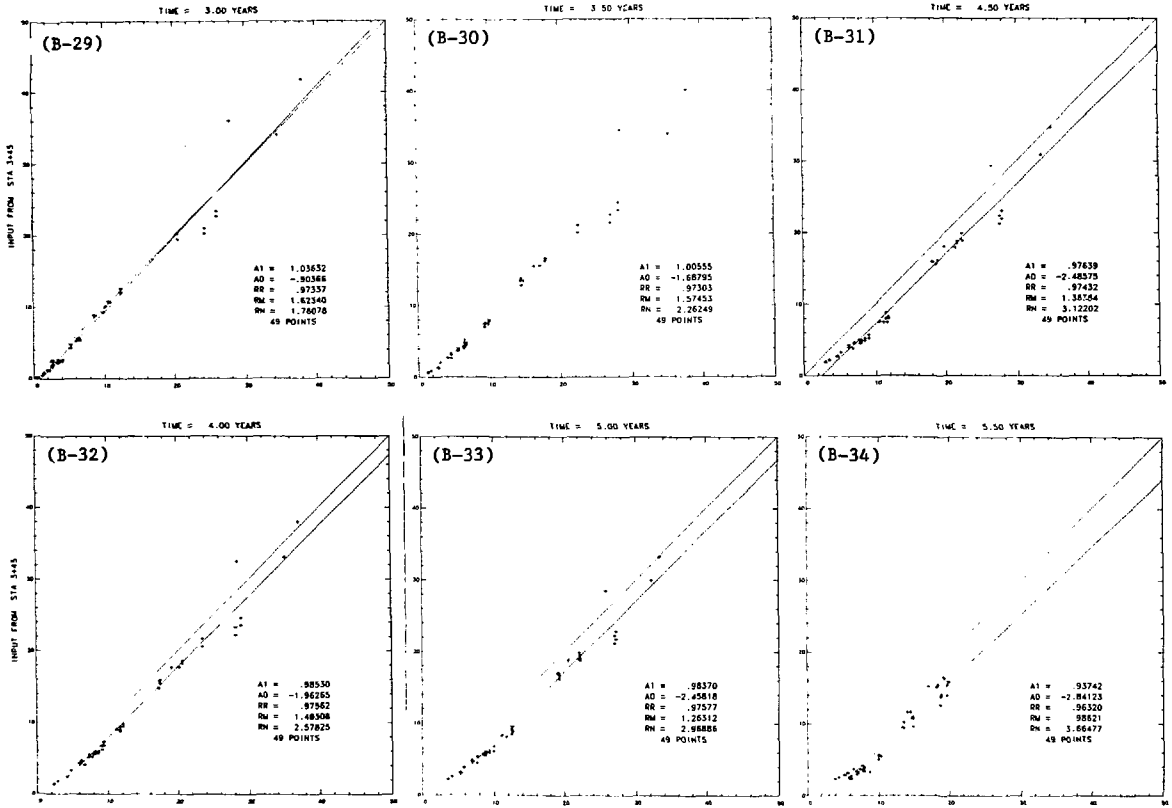

Fig. B-29 through B-34. Measured vs calculated (CN1195) temperature rises at 3.00, 3.50, 4.00, 4.50, 5.00, 5.50 YOC, station 3+45.

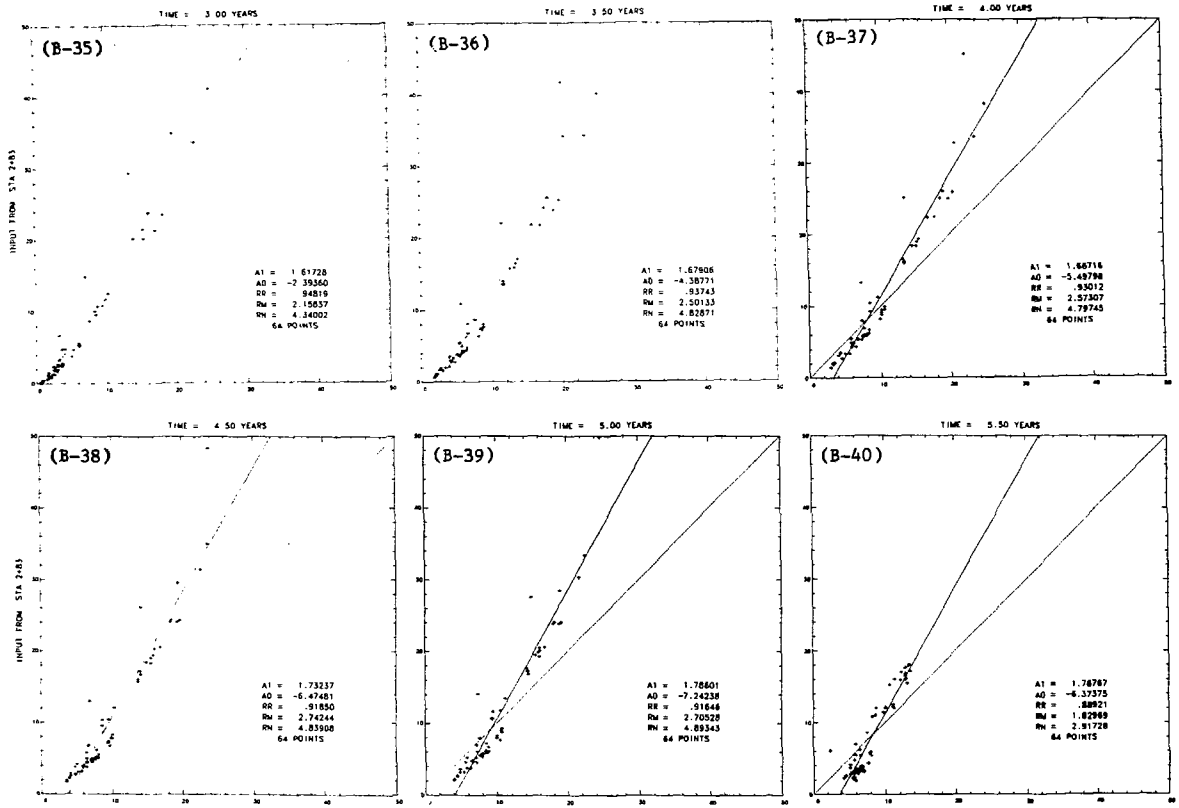

Fig. B-35 through B-40. Measured vs calculated (CN1196) temperature rises at 3.00, 3.50, 4.00, 4.50, 5.00, 5.50 YOC, station 2+83.

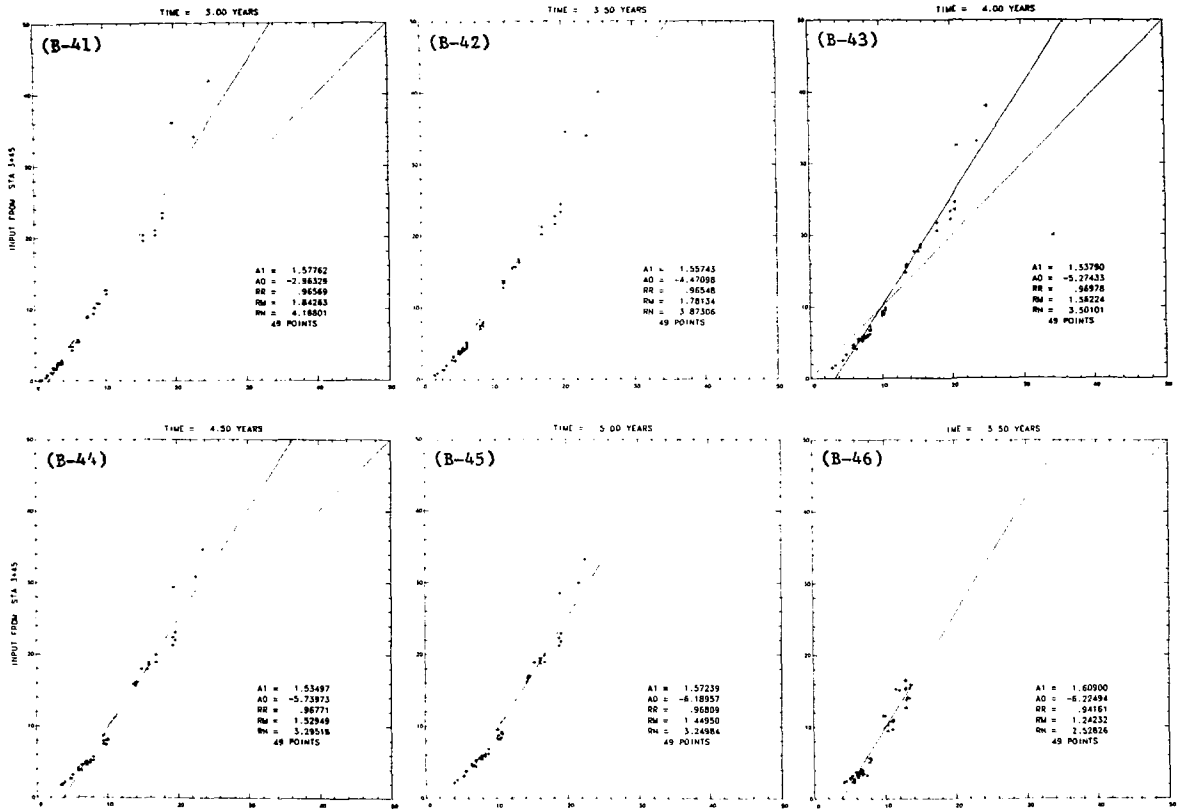

Fig. B-41 through B-46. Measured vs calculated (CN1196) temperature rises at 3.00, 3.50, 4.00, 4.50, 5.00, 5.50 YOC, station 3+45.

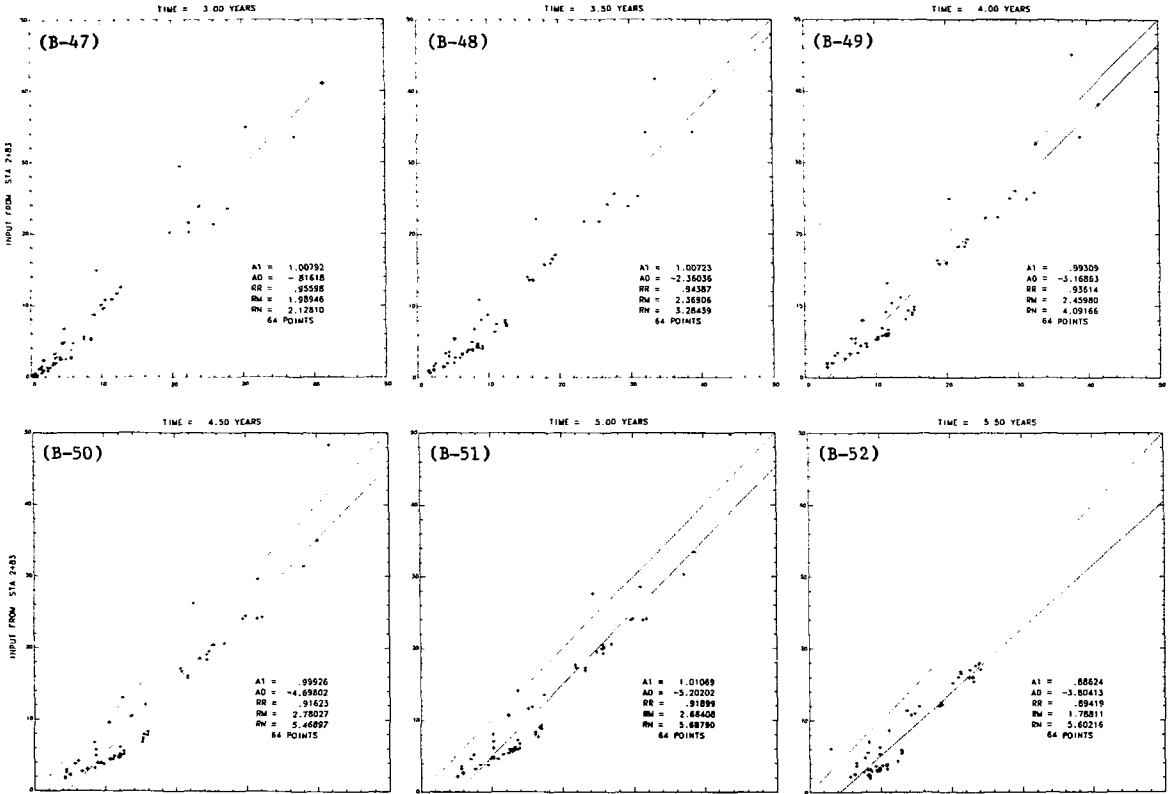

Fig. B-47 through B-52. Measured vs calculated (CN1197) temperature rises at 3.00, 3.50, 4.00, 4.50, 5.00, 5.50 YOC, station 2+83.

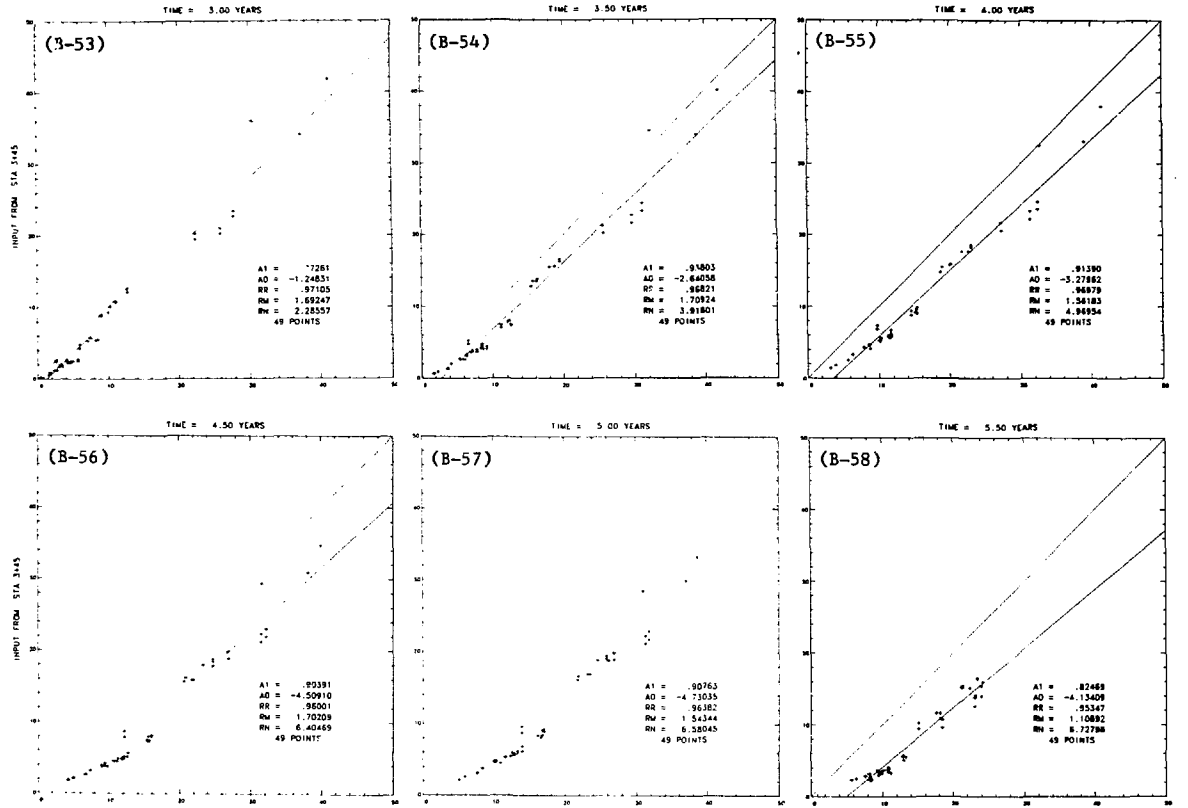

Fig. B-53 through B-58. Measured vs calculated (CN1197) temperature rises at 3.00, 3.50, 4.00, 4.50, 5.00, 5.50 YOC, station 3+45.

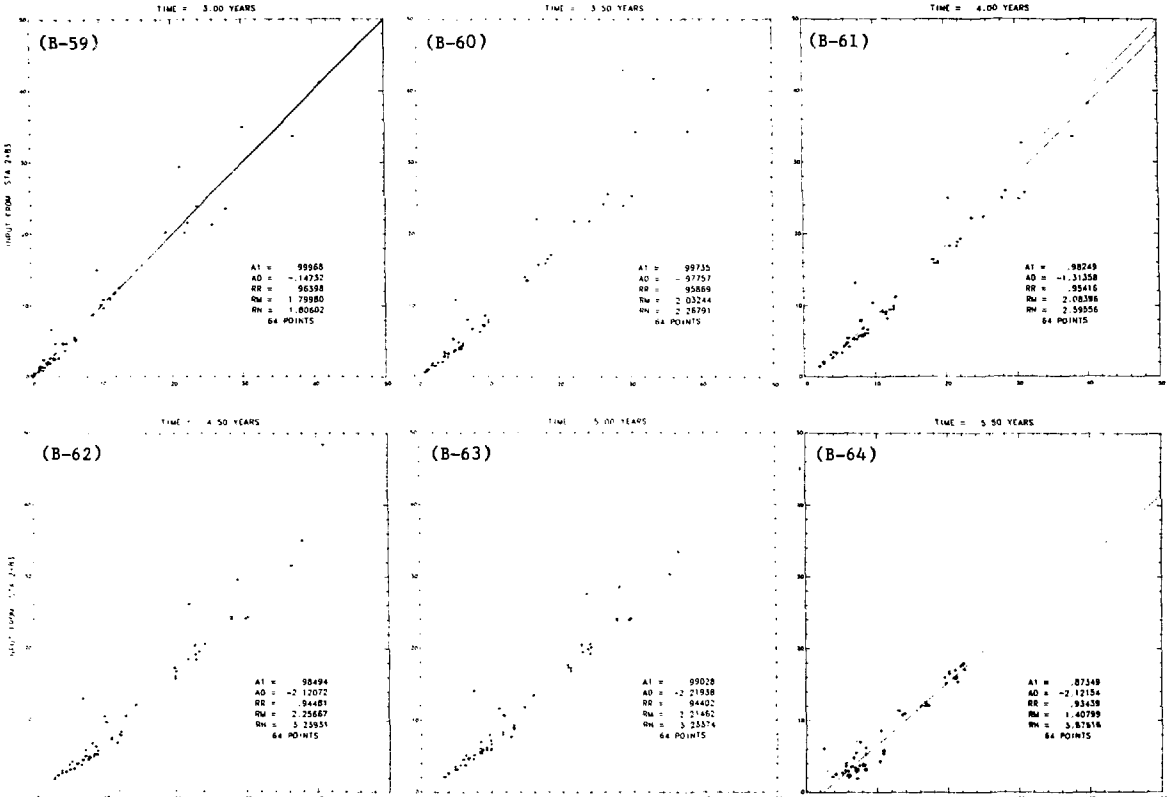

Fig. B-59 through B-64. Measured vs calculated (CN1199) temperature rises at 3.00, 3.50, 4.00, 4.50, 5.00, 5.50 YOC, station 2+83.

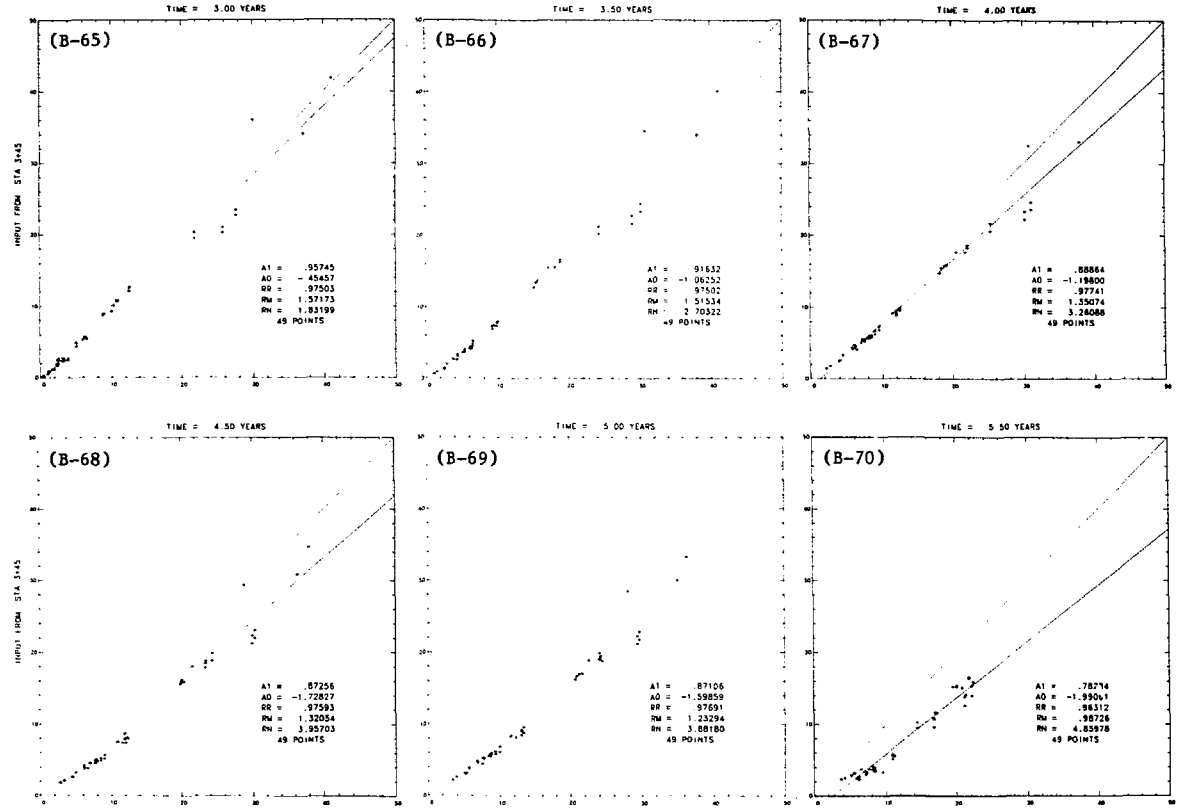

Fig. B-65 through B-70. Measured vs calculated (CN1199) temperature rises at 3.00, 3.50, 4.00, 4.50, 5.00, 5.50 YOC, station 3+45.

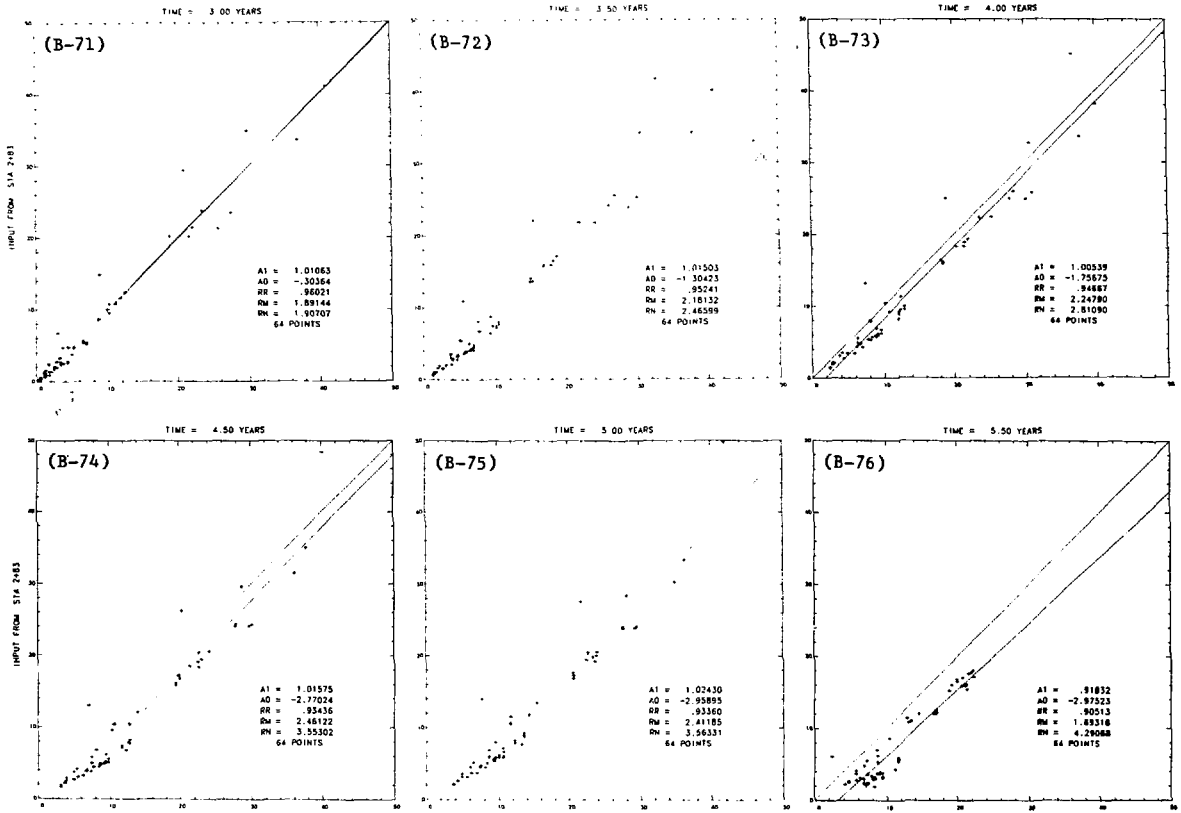

Fig. B-71 through B-76. Measured vs calculated (CN1200) temperature rises at 3.00, 3.50, 4.00, 4.50, 5.00, 5.50 YOC, station 2+83.

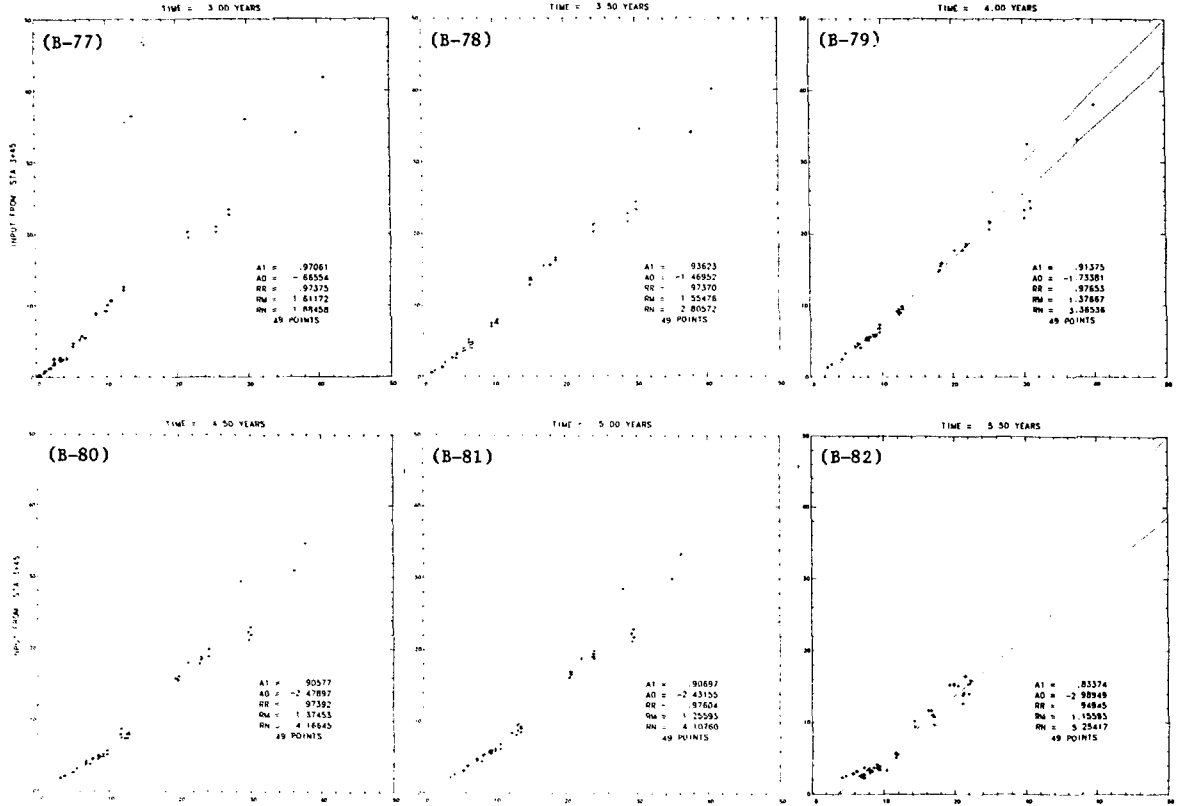

Fig. B-77 through B-82. Measured vs calculated (CN1200) temperature rises at 3.00, 3.50, 4.00, 4.50, 5.00, 5.50 YOC, station 3+45.

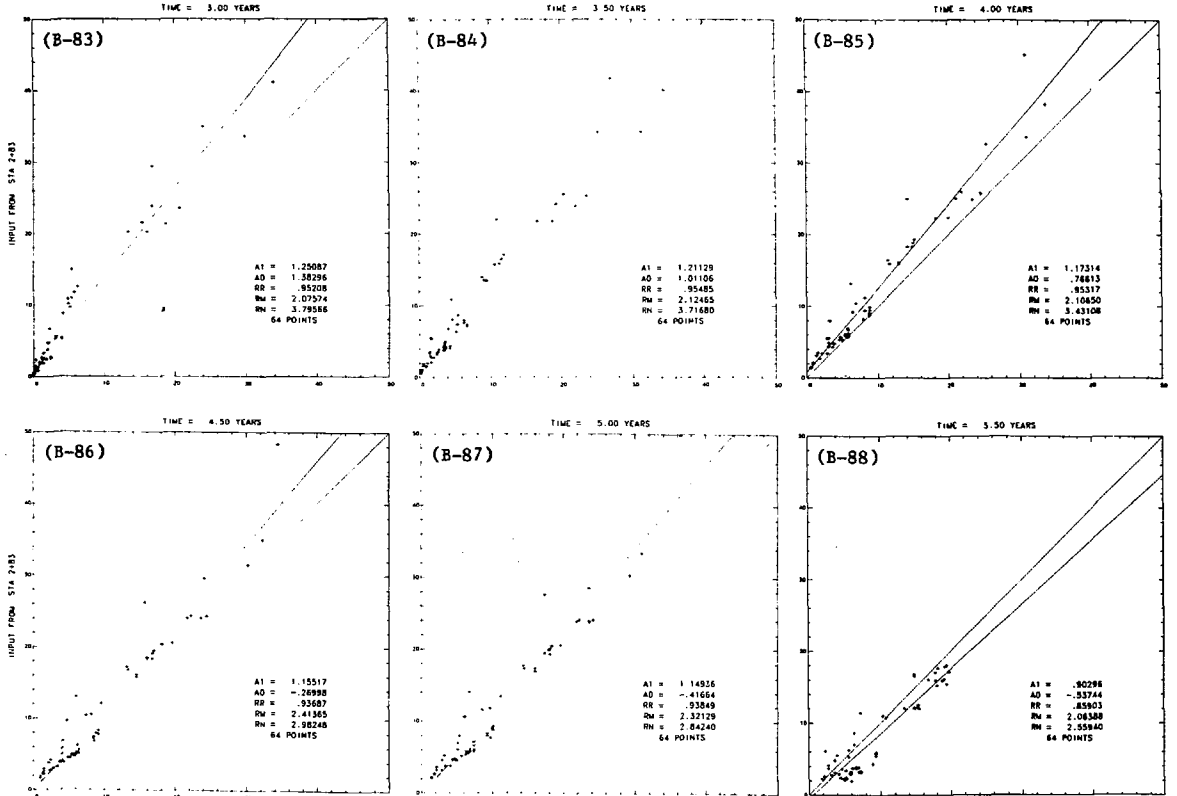

Fig. B-83 through B-88. Measured vs calculated (CN1201) temperature rises at 3.00, 3.50, 4.00, 4.50, 5.00, 5.50 YOC, station 2+83.